How oblique extension and structural inheritance influence rift segment interaction: Insights from 4D analog models

Frank Zwaan[1] and Guido Schreurs[1]

Abstract

Rifting of the continental lithosphere involves the initial formation of distinct rift segments, often along preexisting crustal heterogeneities resulting from preceding tectonic phases. Progressive extension, either orthogonal or oblique, causes these rift segments to interact and connect, ultimately leading to a full-scale rift system. We study continental rift interaction processes with the use of analog models to test the influence of a range of structural inheritance (seed) geometries and various degrees of oblique extension. The inherited geometry involves main seeds, offset in a right-stepping fashion, along which rift segments form as well as the presence or absence of secondary seeds connecting the main seeds. X-ray computer tomography techniques are used to analyze the 3D models through time, and results are compared with natural examples. Our experiments indicate that the extension direction exerts a key influence on rift segment interaction. Rift segments are more likely to connect through discrete fault structures under dextral oblique extension conditions because they generally propagate toward each other. In contrast, sinistral oblique extension commonly does not result in hard linkage because rift segment tend to grow apart. These findings also hold when the system is mirrored: left-stepping rift segments under sinistral and dextral oblique extension conditions, respectively. However, under specific conditions, when the right-stepping rift segments are laterally far apart, sinistral oblique extension can produce hard linkage in the shape of a strike-slip-dominated transfer zone. A secondary structural inheritance between rift segments might influence rift linkage, but only when the extension direction is favorable for activation. Otherwise, propagating rifts will simply align perpendicularly to the extension direction. When secondary structural grains do reactivate, the resulting transfer zone and the strike of internal faults follow their general orientation. However, these structures can be slightly oblique due to the influence of the extension direction. Several of the characteristic structures observed in our models are also present in natural rift settings such as the Rhine-Bresse Transfer Zone, the Rio Grande Rift, and the East African Rift System.

Introduction

During the early stages of rifting, rift segments generally form along preexisting lithospheric weaknesses formed during previous tectonic activity (Morley et al., 1990; Nelson et al., 1992; Corti, 2012). Because these weaknesses are often noncontinuous, the initial rift segments distributed in loose and in-line or en echelon arrangements (Morley et al., 2004) and need to interact and connect to form a continuous rift system. Associated rift linkage structures are classified as either transfer zones (TZs) when a discrete fault system connects both rift segments (hard linkage) or accommodation zones (soft linkage) when deformation is distributed and faults do not connect (Rosendahl, 1987; Larsen, 1988; Childs et al., 1995; Faulds and Varga, 1998; Figure 1e and 1f). The complex evolution and structuration of rift interaction zones has an important influence on sedimentary facies distribution and the mi-
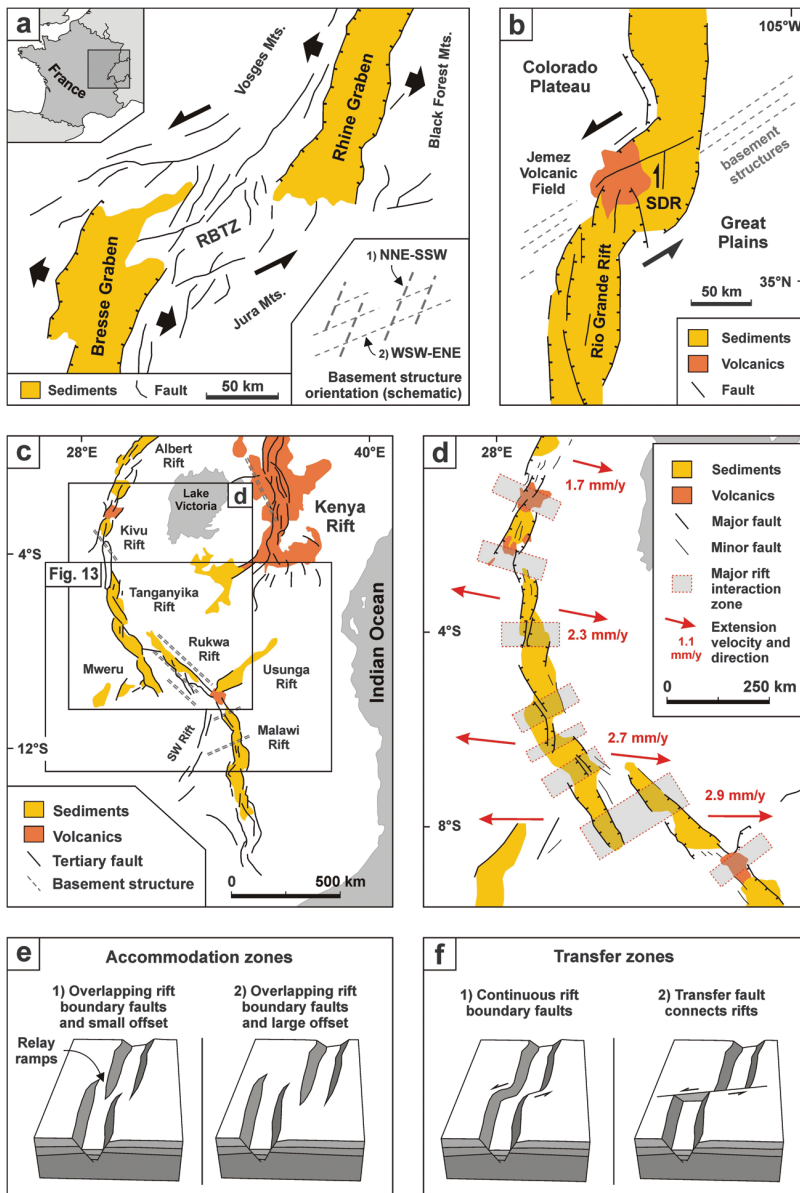
gration and trapping of hydrocarbons (Morley et al., 1990; Paul and Mitra, 2013). Several hydrocarbon fields are associated with accommodation zones in, e.g., the North Sea Viking Graben (Fossen et al., 2010). Interacting rift segments also influence magma migration and vice versa (Corti et al., 2004; Minor et al., 2013). Other examples of rift interaction zones are found in, e.g., Eastern France (Rhine-Bresse Transfer Zone [RBTZ]; Illies, 1977; Ustaszewski et al., 2005; Figure 1a), the Utah Canyonlands (accommodation zones, Trudgill and Cartwright, 1994; Fossen et al., 2010), New Mexico, USA (Santo Domingo Relay [SDR] in the Rio Grande Rift; Aldrich, 1986; Minor et al., 2013; Figure 1b), and the East African Rift System (various transfer and accommodation zones; Morley et al., 1990; Corti, 2012; Figure 1c and 1d).

Data from numerical and analog studies indicate the influence of various parameters on rift interaction,

Figure 1. Natural examples of rift interaction structures and accommodation/transfer zone convention. (a) Rhine-Bresse Transfer Zone (RBTZ) between the Rhine Graben and Bresse Graben in eastern France. Image modified after Illies (1977) and Ustaszewski et al. (2005). (b) Santo Domingo Relay (SDR) within the Rio Grande Rift (USA). Image modified after Aldrich (1986) and Minor et al. (2013). (c) East African Rift System depicting the various rift segments and the occurrence of sediment basins and volcanics. Image modified after Ebinger (1989) and Acocella et al. (1999). (d) Western branch of the East African Rift System, showing the major rift interaction zones with the associated sediments and volcanics, as well as current extension directions and velocities. Image modified after Saria et al. (2014) and Corti (2012), the location is shown in (c). Hatched lines represent normal faults; the character of faults without motion indications are not specified in the original publications. (e and f) Block diagrams depicting the differences between accommodation and TZs as proposed by Faulds and Varga (1998). (e) Accommodation zones (soft linkage) in which rift boundary faults do not connect, but die out laterally and overlap. Examples are present in the East African Rift System; their locations are shown in (d). (f) TZs (hard linkage) in which the rift boundary faults are continuous from rift to rift, e.g., the Selenga accommodation zone in Lake Baikal (Scholz and Hutchinson, 2000) or in which a single transfer fault connects both basins, e.g., the Gulf of Suez or Thailand (Acocella et al., 1999; Morley et al., 2004).

e.g., the presence and geometry of structural heterogeneities, such as fault and shear zones, detachment layers, and magma intrusions that determine what structures develop (Elmohandes, 1981; Naylor et al., 1994; Acocella et al., 1999, 2005; Basile and Brun, 1999; Le Calvez and Vendeville, 2002; McClay et al., 2002; Tentler and Acocella, 2010; Paul and Mitra, 2013; Brune, 2014; Zwaan et al., 2016). Key factors affecting the large-scale evolution of rift interaction structures are the rift offset and the degree of brittle-ductile coupling in the system. Larger offsets between rift segments cause TZs to be narrower (Acocella et al., 1999; Dauteuil et al., 2002) or even prevent TZs from developing (Le Calvez and Vendeville, 2002; Allken et al., 2011, 2012; Zwaan et al., 2016). However, initial accommodation zones tend to evolve into TZs with increasing deformation (Acocella et al., 2005) and higher strain rates increase transfer zone widths (Dauteuil et al., 2002). The overlap or underlap of rift segments (see also Figure 2d, 2e, and 2i) can result in a variation of rift interaction zone structures and can cause the formation of microcontinents (Müller et al., 2001; Tentler and Acocella, 2010). In addition, strong brittle-ductile coupling due to either high viscosities in the lower crust or high extension velocities (Brun, 1999; Buiter et al., 2008) causes distributed deformation (wide rifting) and prevents rift segments from developing discrete transfer zones (Allken et al., 2011, 2012; Zwaan et al., 2016).

Recent numerical modeling suggests that oblique extension, i.e., when the extension direction is not orthogonal to the strike of a structure (Figure 2f), is an important factor promoting continent break up (Brune et al., 2012; Bennett and Oskin, 2014). Although oblique extension has been studied and modeled extensively with respect to the evolution of continuous rifts (Tron and Brun, 1991; McClay and White, 1995; Clifton and Schlische, 2001; McClay et al., 2002; Brune, 2014; Philippon et al., 2015), its effects on interacting rift segments have largely been neglected to date. In our previous analog modeling study (Zwaan et al., 2016), we did apply various degrees of dextral oblique extension and various seed offsets. The offset was of the "staircase" type (no over- or underlapping seeds),

and the seeds that localize deformation were not linked by any secondary structural weakness. We demonstrated how dextral oblique extension and low seed offsets promote rift linkage, what structures can be expected, and how these evolve. Here, we elaborate on our earlier work by assessing the effects of both the geometry of inherited structures (linked and not linked with various degrees of under- and overlap) and of oblique extension (sinistral and dextral) on rift interaction processes.

Contrary to most previous analog models, we use a model setup with distributed basal deformation that allows us to apply a greater variety of structural inheritance geometry because we do not force deformation along the edges of a baseplate (see also Morley, 1999; Le Calvez and Vendeville, 2002; Zwaan et al., 2016 and compare with Elmohandes, 1981; Acocella et al., 1999; Basile and Brun, 1999; Dauteuil et al., 2002). Selected models were analyzed by X-ray computer tomography (CT) techniques to reveal their detailed internal and external structures in 4D.

Materials and methods
Model setup

We use a similar methodology as applied by Zwaan et al. (2016, Figure 2). Our models are designed to represent the continental crust: Alternations of quartz and corundum sand (grain size of 60–250 μm, density of 1560 kg/cm^3; grain size of 88–175 μm, density of 1890 kg/cm^3, respectively) form the model brittle upper crust. This alternation of sands with different densities serves to create X-ray attenuation variations that permit the visualization of model layers on CT images (Figure 2g). The quartz and corundum sands have an internal peak friction angle of 36.1° and 37° and cohesion values of approximately 9 and 39 Pa, respectively. A near-Newtonian viscous mixture of corundum sand and silicone (SGM-36 PDMS) represents the ductile lower crust onto which the sand layers are sieved from an height of ca. 30 cm. The brittle and ductile model layers are both 2 cm thick, and the total 4 cm layer cake translates to a 40 km thick continental crust. For CT-scanned models, we use a double layer thickness (8 cm total) to better visualize structural details. Further details of the model materials are given in Table 1.
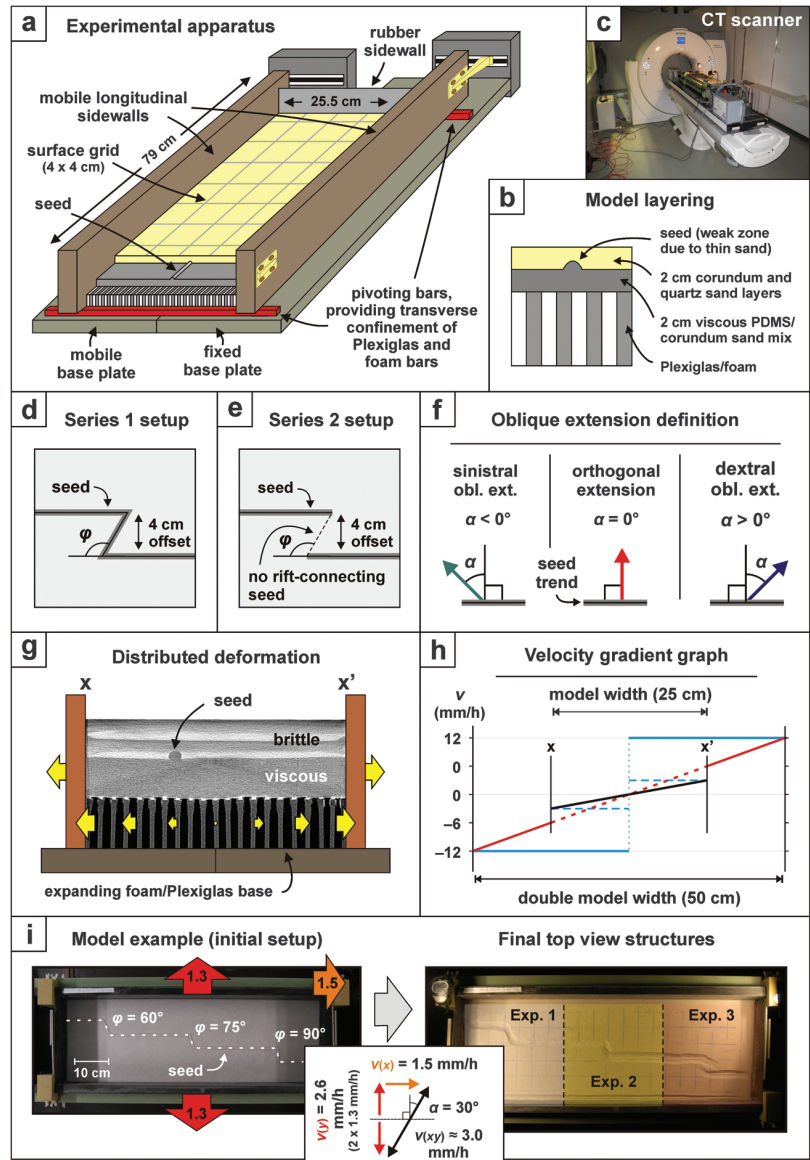
Figure 2. Model setup. (a) Cut-out view of the experimental apparatus depicting its various components. (b) Compositional layering of quartz and corundum sand representing the brittle upper crust and a viscous silicone/corundum sand mixture simulating the ductile lower crust, above a Plexiglas and foam base. (c) Experimental apparatus in the CT scanner during a model run. (d and e) Seed geometry setup for our two model series with a secondary rift-connecting seed (series 1) and without a secondary seed (series 2). (f) Extension obliquity definition for our model series. (g) Distribution basal deformation in the model. As the sidewalls move apart with 3 mm/h, a velocity gradient develops in the foam and Plexiglas base (yellow arrows). The CT image is derived from model B (compare with Figure 6). Layering in the sand is due to the alternations of quartz and corundum sand with different densities. (h) Velocity gradient due to the distributed basal deformation in our setup. The standard 3 mm/h velocity gradient for the normal model width (black line) would have to be quadrupled for a model with double dimensions (red line). However, as our models with double layer thickness have the same width as our standard models, the velocity should only be doubled to obtain the correct velocity gradient (dotted red line). The model velocity is kept at 3 mm/h for the CT-scanned models, but as explained in the text, the model structures are still comparable. For comparison, the blue lines show the velocity profile for basal plate setups with a normal thickness (dotted blue line) and a double thickness (continuous blue line). (i) Example of a model run. (Left) Initial setup of three separate experiments in one model run (without sand cover). (Right) Final surface structures.

Our experimental apparatus contains a 30.5 cm wide base of 20 foam and 21 Plexiglas bars (each 1.0 and 0.5 cm wide, respectively) that is compressed to a 25.5 cm width between two mobile sidewalls (Figure 2a). By moving the sidewalls apart, the foam expands uniformly resulting in a distributed extensional deformation in the overlying model materials. The mechanism can be considered to be the active rifting type because deformation is controlled by extension at the base of the model, rather than by "far-field stresses" due to pull by the opening sidewalls. In addition, one of the baseplates can move laterally. This allows us to model strike-slip settings and, in combination with orthogonal extension, to apply oblique extension. In these oblique extension models, additional transverse sidebars guide the shearing of the foam and Plexiglas bars at the base of the model setup.

On top of the basal PDMS/corundum sand layer, we apply ca. 5 mm wide, 2.5 mm high semicircular bulges (seeds) of the same viscous mixture. These seeds represent the influence of discrete inherited weaknesses (e.g., faults or shear zones) that localize deformation because the strong overlying sand is locally thinner (Figure 2b). Structural weaknesses in nature may also occur as pervasive fabrics, i.e., present over a wide area (e.g., a dominant foliation), which poses an important challenge to analog modelers (Morley, 1999). However, the natural examples we address in this paper can be considered of the discrete type on the crustal scale we are concerned with (examples in Figure 1). The seeds serve to create right-stepping rift segments at the desired locations (Figure 2d, 2e, and 2i). Our rift segments are relatively narrow though, due to the narrow seed and basic rift geometry (Allemand and Brun, 1991). Other modelers have often applied wider patches of silicone (Tron and Brun, 1991) or a rubber base sheet (McClay and White, 1995), of which the edges determine the rift boundaries, producing wider rifts with more detailed structures. However, since we focus on large-scale rift interaction processes instead of detailed structuration, this is acceptable. An advantage over traditional analog setups with baseplates (Elmohandes, 1981; Acocella et al., 1999; Basile and Brun, 1999; Dauteuil et al., 2002) is that our setup allows a large variation of structural inheritance geometries; the seeds can be applied in any desired geometry. We also exploit the length of the experimental apparatus to increase our model efficiency by running three experiments per model run (Figure 2i).

We use the term H that is equal to the thickness of the brittle crust (Allken et al., 2011, 2012) to quantify lengths in our models. The brittle crust thickness has a major influence on rift geometry (Allemand and Brun, 1991), and this normalized value H enables comparisons between models with different brittle layer thicknesses. The horizontal offset between the seeds is set at 2 H (4 cm in the normal thickness models and 8 cm in the CT-scanned models), to cancel any rift-proximity effects observed previously by Zwaan et al. (2016). We define seed over- and underlap by the angle ϕ between the main seed trend and the orientation of the line between the near ends of the seeds (Figure 2d and 2e). Extension obliquity is given by the angle α between the normal to the rift trend and the extension direction (Figure 2f). A negative angle α represents a situation with sinistral oblique extension, whereas a positive angle indicates dextral oblique extension. When angle α is 0°, extension is orthogonal. We apply an extension velocity of 3 mm/h to better localize deformation, eliminating the effects due to high brittle-ductile coupling and the associated wide rifting (Brun, 1999; Buiter et al., 2008; Figure A-1). As it is standard in most physical rifting models, the extension rate is constant along the whole length of our models. Models run for 8 h, producing 2.4 cm of extension in the given extension direction.

The 47 models run for this study are split into two series (Table 2). The models in the first series are aimed at investigating the effect of a secondary seed connecting the parallel-oriented main lateral seeds. This rift-connecting seed represents a secondary discrete structural inheritance as observed in, e.g., Eastern France (Ustaszewski et al., 2005; Figure 1a), the Santo Domingo Relay (SDR) in the Rio Grande Rift in the USA (Acocella et al., 1999; Figure 1b), and the East African Rift System (Acocella et al., 1999; Corti, 2012). In series 1 models, the main seeds are arranged in a right-stepping fashion and we model geometries with under- and overlap (Figure 2d). Next to the dextral oblique extension and orthogonal extension previously applied by Zwaan et al. (2016), we also apply sinistral oblique extension, as observed in, e.g., the East African Rift System (Saria et al., 2014). Note that not all combinations of extension direction and seed geometry

Table 1. Material properties.

Granular materials	Quartz sand	Corundum sand
Grain size range	60–250 μm	88–175 μm
Density (sieved)	1560 kg/m³	1890 kg/m³
Angle of internal peak friction	36.1°	37°
Angle of dynamic-stable friction	31.4°	32°
Cohesion	9 ± 98 Pa	39 ± 10 Pa
Viscous material	PDMS/corundum sand mixture	
Weight ratio PDMS : corundum sand	0.965 : 1.00 kg	
Mixture density	ca. 1600 kg/m³	
Viscosity[a]	ca. 1.5×10^5 Pa · s	
Type	Near-Newtonian ($n = 1.05$)[b]	

[a]The viscosity value holds for model strain rates $<10^{-4}$ s^{-1}.
[b]Stress exponent n (dimensionless) represents sensitivity to strain rate.

Table 2. Overview of model parameters

Series 1 (with rift-connecting seed)				Series 2 (without rift-connecting seed)			
Model no.	Extension obliquity (angle α)	Seed geometry (angle ϕ)	Shown in	Model no.	Extension obliquity (angle α)	Seed geometry (angle ϕ)	Shown in
1	−30°	60°	Figure 4	**27 (C)**[a]	−30°	30°	Figure 9
2	−30°	75°	Figure 4	**28 (D)**[a]	−30°	30°	Figure 9
3	−30°	90°	Figure 4	**29 (E)**[a]	−30°	30°	Figure 9
4	−30°	105°	Figure 4	30	−30°	15°	Figure 8
5	−30°	120°	Figure 4	31	−30°	45°	Figure 8
6	−30°	135°	Figure 4	32	−30°	60°	Figure 8
7 (G)[a]	−30°	30°	Figure 9	33	−30°	90°	Figure 8
8	0°	60°	Figure 4	34	0°	15°	Figure 8
9	0°	75°	Figure 4	35	0°	30°	Figure 8
10	0°	90°	Figure 4	36	0°	45°	Figure 8
11	0°	105°	Figure 4	37	0°	60°	Figure 8
12	0°	120°	Figure 4	38	0°	75°	Figure 8
13	0°	135°	Figure 4	39	0°	90°	Figure 8
14	30°	60°	Figure 4	40	30°	15°	Figures 8 and A-1
15	30°	75°	Figure 4	41	30°	45°	Figures 8 and A-1
16	30°	90°	Figure 4	42	30°	90°	Figures 8 and A-1
17	30°	105°	Figure 4	**43 (F)**[a, b]	−30°	30°	Figures 9–11 and 13
18	30°	120°	Figure 4	44[c]	30°	90°	Figure A-1
19	30°	135°	Figure 4	45[c]	30°	±15°	Figure A-1
20	60°	60°	Figure 4	46[c]	30°	±30°	Figure A-1
21	60°	75°	Figure 4	47[c]	30°	±55°	Figure A-1
22	60°	90°	Figure 4	—	—	—	—
23	60°	105°	Figure 4	—	—	—	—
24 (A)[a]	60°	120°	Figures 3 and 4	—	—	—	—
25	60°	135°	Figure 4	—	—	—	—
26 (B)[a, b]	15°	75°	Figures 5–7	—	—	—	—

[a](Bold): key models, referred to as models A–G in the text.
[b]CT-scanned models.
[c]Models with a 6 mm/h extension velocity instead of the standard 3 mm/h.

Table 3. Scaling parameters.

	General parameters			Brittle upper crust		Ductile lower crust		Dynamic scaling values	
	Gravitational acceleration g (m/s^2)	Crustal thickness h (m)	Extension velocity v (m/s)	Density ρ (kg/m^3)	Cohesion C (Pa)	Density ρ (kg/m^3)	Viscosity η (Pa · s)	Ramberg number R_m	Brittle stress ratio R_s
Model (normal)	9.81	0.04	8.3×10^{-7}	1690[a]	24[b]	1600	1.5×10^5	25	13.8
Model (CT)	9.81	0.08	8.3×10^{-7} (1.7×10^{-6})[c]	1690[a]	24[b]	1600	1.5×10^5	100	27
Nature	9.81	4×10^4	ca. 1×10^{-10}	2800	7×10^{7d}	2900	$1 \times 10^{19-23e}$	$1 \times 10^{0\,to\,4}$	9.2

[a]Average density of both sand types.
[b]Average cohesion of both sand types.
[c]Virtual velocity for a double model width (see the text for explanation).
[d]Cohesion value after Corti et al. (2004).
[e]Viscosity range after Buck (1991).

are necessarily found in nature, but this way, we create a complete and systematic overview of the structures we can expect as a result of the combined effects of rift under/overlap and various degrees of oblique extension.

The models in the second series consist of parallel-oriented, right-stepping main seeds without secondary rift-connecting seeds, leaving the system more freedom to evolve between the main rifts (Figure 2e). These series 2 models focus on main seeds with underlap only, but they do involve sinistral and dextral oblique extensions as in series 1. Also in this series, not every model should necessarily have an equivalent in nature. Further factors, such as the effects of sedimentation and erosion, are not considered in this study.

Model scaling

The Mohr-Coulomb characteristics of sand enable its use as an analog for the brittle crust. Viscous materials are more complex to apply because of their time-dependent behavior. We use the density, length, and gravity ratios (ρ^*, h^*, and g^*, respectively, convention: $\rho^* = \rho_{model}/\rho_{nature}$) to calculate stress ratios: $\sigma^* = \rho^* \cdot h^* \cdot g^*$ (Hubbert, 1937; Ramberg, 1981). Subsequently, we calculate the strain rate ratio with the viscosity ratio (η^*): $\dot{\varepsilon}^* = \sigma^*/\eta^*$ (Weijermars and Schmeling, 1986). Next, velocity and time ratios (v^* and t^*) are obtained: $\dot{\varepsilon}^* = v^*/h^* = 1/t^*$. Depending on the assumed viscosity of the lower crust, our 3 mm/h model velocity and our 4 cm model representing a 40 km thick continental crust

translates to a velocity between ca. 7×10^{-2} and 7×10^2 mm/year in nature. Velocities measured in natural rift settings plot in this range (e.g., a few mm/year in East Africa; Saria et al., 2014).

Further scaling formulas concern the dynamic similarity between models and nature. The ratio R_s between gravitational stress and cohesive strength (cohesion C) applies to the brittle domain: $R_s = \text{gravitational stress}/\text{cohesive strength} = \rho \cdot g \cdot h/C$ (Ramberg, 1981; Mulugeta, 1988). Similarly, the Ramberg number R_m or ratio between gravitational forces and viscous stress relates to the viscous domain: $R_m = \text{gravitational stress}/\text{viscous stress} = \rho \cdot g \cdot h/(\dot{\varepsilon} \cdot \eta) = \rho \cdot g \cdot h^2/(\eta \cdot v)$ (Weijermars and Schmeling, 1986). The R_s value of 13.8 for the model is close to the natural value of 9.2, whereas the model R_m of 50 fits in the natural range (1 to 1×10^4). We therefore consider our standard 4 cm thick models to be properly scaled. Scaling parameters are summarized in Table 3.

The double thickness in the CT-scanned models (8 cm instead of 4 cm) has some consequences for scaling. Following the scaling equations, the model extension velocity should be quadrupled to account for a double layer thickness. This is, however, only valid in a standard rigid baseplate model with a constant extension velocity throughout the model (the blue lines in Figure 2h). In contrast, the extension velocity in our model follows a gradient (Figure 2g and 2h). As the model width remains the same as in our standard thickness models, the extension velocity at the edge of the model should only be doubled to 6 mm/h (the red lines in Figure 2h). Only when the model width would be doubled too, should the extension velocity be quadrupled (the blue and red lines intersecting in Figure 2h). The extension velocity for the CT models is, however, kept at 3 mm/h instead of raising it to 6 mm/h (the black line in Figure 2h). These 3 mm/h at the edge of the model, or rather the virtual 6 mm/h for a double model width, correspond to an extension velocity between 3.6×10^{-2} and 3.6×10^2 mm/year in nature. This velocity range still captures natural plate velocities. The R_s and R_m ratios are now 27 and 100, respectively. The former is still close to the natural value, and the latter still fits in the natural range between 1 and 1×10^4. Because the structures we observe with the standard and double model thicknesses are quite similar, we consider them comparable.
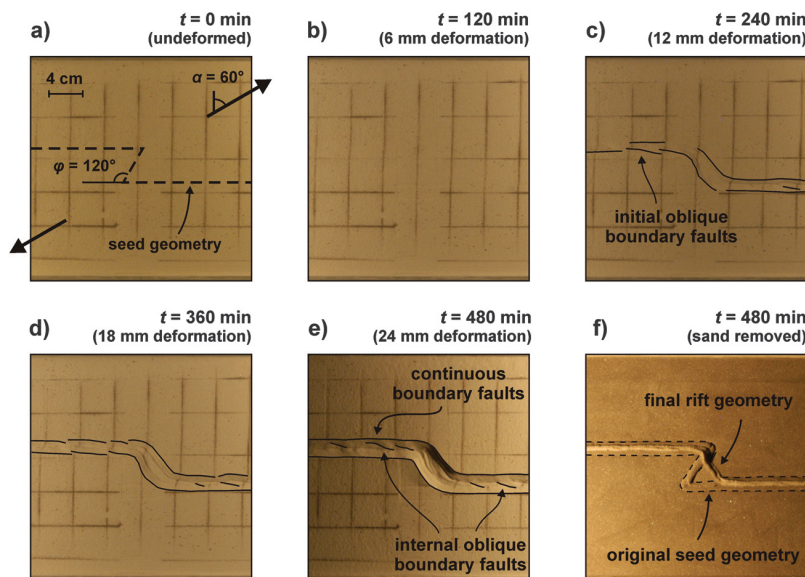
Figure 3. Top-view images depicting the evolution of model A from series 1 (with rift-connecting seed). (a) Initial setup with seed geometry and extension direction: angle $\phi = 120°$ (overlap) and angle ($\alpha = 60°$ (dextral oblique extension). The 4×4 cm surface grid allows the assessment of surface motion. (b-e) Surface evolution of the model. (f) Initial seed geometry (within the dotted lines) and the actual orientation of the transfer zone at the end of the model run and after removal of the sand layers. The transfer zone orientation is visible due to the isostatic rising of the viscous layer associated with decreased loading as the basin formation thins the overlying sand layer.

Results series 1
Series 1: General overview

Faults only become visible on top-view images after enough topography has

formed to cast shadows on the obliquely lit model surface, although CT scanning shows fault formation shortly after model initiation in this type of model (Zwaan et al., 2016). Consequently, the first structures appear on the top-view images after some 6 mm (0.3 H) of extension (model A, Figure 3b) and continue to evolve until the end of the model run when 24 mm (1.2 H) of extension has taken place (Figure 3e).

We present an overview of the final surface structures from series 1, in which the main seeds are connected by a secondary inherited weakness with various orientations (angles ϕ). We apply a spectrum of extension directions including dextral and sinistral oblique extension, as well as pure orthogonal extension (angle α ranges between $-30°$ and $60°$; Figure 4). All 24 models produce well-developed rift segments above the main lateral seeds with a symmetric graben structure whose width decreases with increasing extension obliquity (either sinistral or dextral). Rift width is reduced from approxi-

mately 1.5 H (2.9 cm) to 0.95 H (1.9 cm) for angle α increasing from $0°$ to $60°$. We also observe the occurrence of initial en echelon faults that quickly connect with each other to form continuous rift boundary faults when extension is oblique (best visible in Figures 3c–3e and 5c–5f). These rift boundary faults also accommodate increasing amounts of strike-slip motion with increasing degrees of oblique extension: approximately 0.2 H (0.4 cm) for $\alpha = \pm30°$ and 0.5 H (1.0 cm) for $\alpha = 60°$. Within the rift segments, sinistral oblique extension models develop right-stepping en echelon rift-internal faults that accommodate oblique-slip motion (Figure 4a–4f), whereas dextral oblique extension models form left-stepping rift-internal faults (Figure 4m–4x). In some cases, minor (strike-slip) faults develop away from the rift structures (Figure 4s, 4p, and 4r) or at the tips of the rift segments (Figure 4o, 4r, 4s, 4u, and 4v). These minor structures are not considered to have a large influence on the main structures we are interested in. Boundary
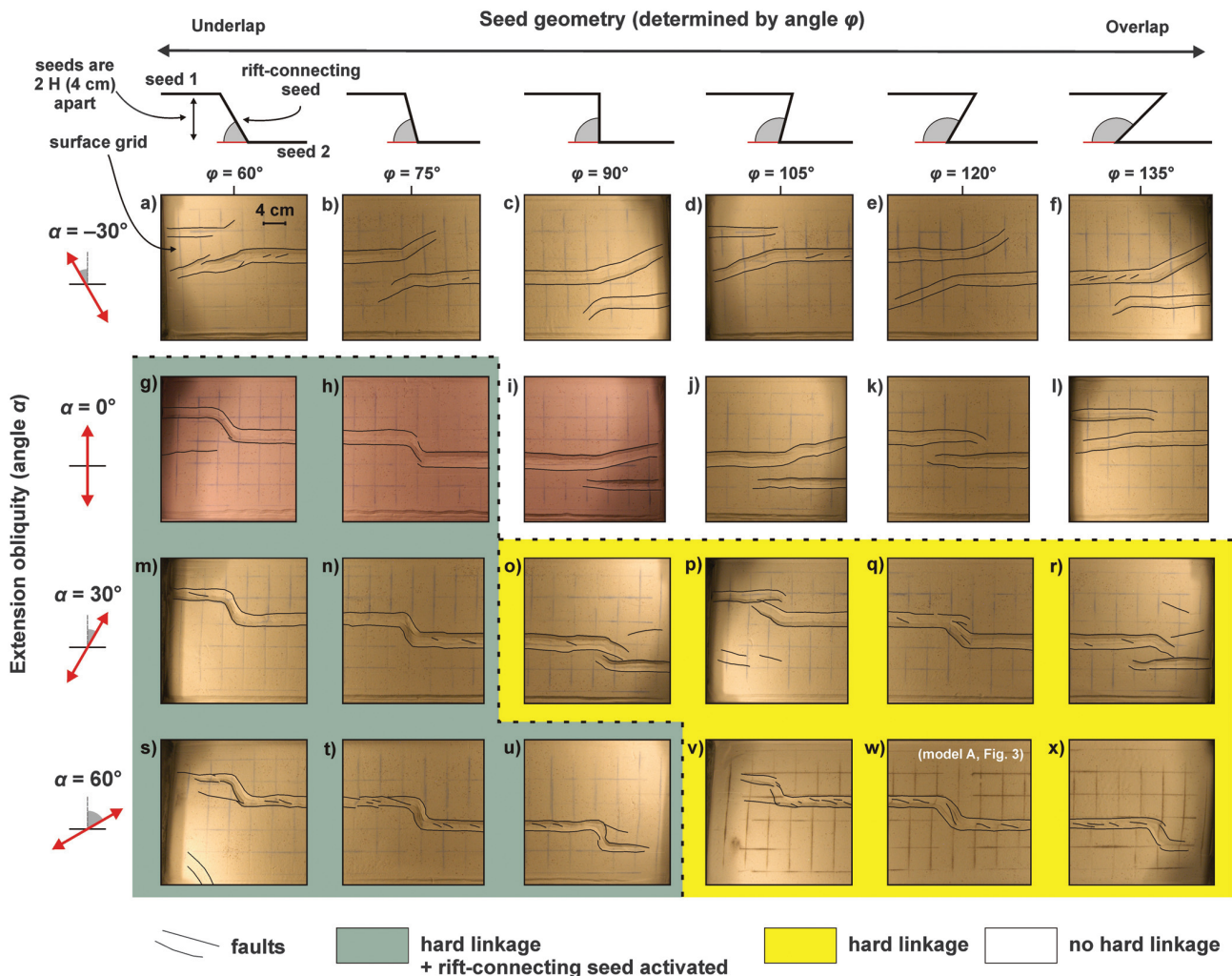
Figure 4. Overview of final surface structures of 24 models from series 1 (with rift-connecting seeds) as a function of extension direction (angle α) and seed geometry (determined by angle ϕ). The models in the overview are divided in three groups: models without hard linkage, i.e., no transfer zone; models with hard linkage, but without activation of the rift-connecting seed; and models with hard linkage and activation of the rift-connecting seed.

effects are mostly restricted to limited normal faulting along the longitudinal sidewalls (Figure 6).

Although every model contains well-developed rift segments along the main seeds, these segments do not connect in all cases: Rifts in −30° (sinistral) oblique extension models propagate subperpendicularly to the extension direction and thus away from each other, regardless of the presence and orientation of the secondary rift-connecting seed (Figure 4a–4f). Models with orthogonal extension only show the development of TZs when angle ϕ is 75° or less (Figure 4g and 4h). Otherwise, the main rift segments propagate in a parallel fashion, subperpendicular to the extension direction (Figure 4i–4l).

In contrast to the sinistral oblique extension models, all dextral oblique extension models exhibit hard linkage and produce TZs (Figure 4m–4x). However, as in the case of their sinistral oblique extension equivalents, the secondary rift-connecting seeds are often not activated. In several cases, they are even crosscut by the propagating rift structures (Figures 3f, 4o–4r, and 4v–4x). Only when the extension obliquity (angle α) is between 0° and 60° and angle ϕ is 90° or less (Figure 4g, 4h, 4m, 4n, and 4s–4u) can we observe activation of the rift-connection seeds. Otherwise, rifts propagate perpendicular to the extension direction, simply ignoring the presence of any rift-connecting seeds.

When TZs develop, they generally consist of curved rift boundary faults that propagate toward the other rift segment, forming a continuous trough that connects both rift segments. The $\alpha = 30°$ and $\phi \geq 90°$ models (Figure 4o–4r) exhibit more complex structures as the rifts propagate from the seed tips and curve around and toward each other. Between both propagating rift branches, a "horst" area remains undeformed and is separated from the main rigid blocks in the model.

Series 1: CT-scanned model (model B)

To further investigate the characteristics of our series 1 models, we ran an $\alpha = 15°$, $\phi = 75°$ model with a rift-connecting seed in the CT scanner (model B). A double layer thickness serves to increase resolution on CT images. In general, the surface structures are similar to the previous models with $\phi = 75°$ and $\alpha = 0°$ or 30°
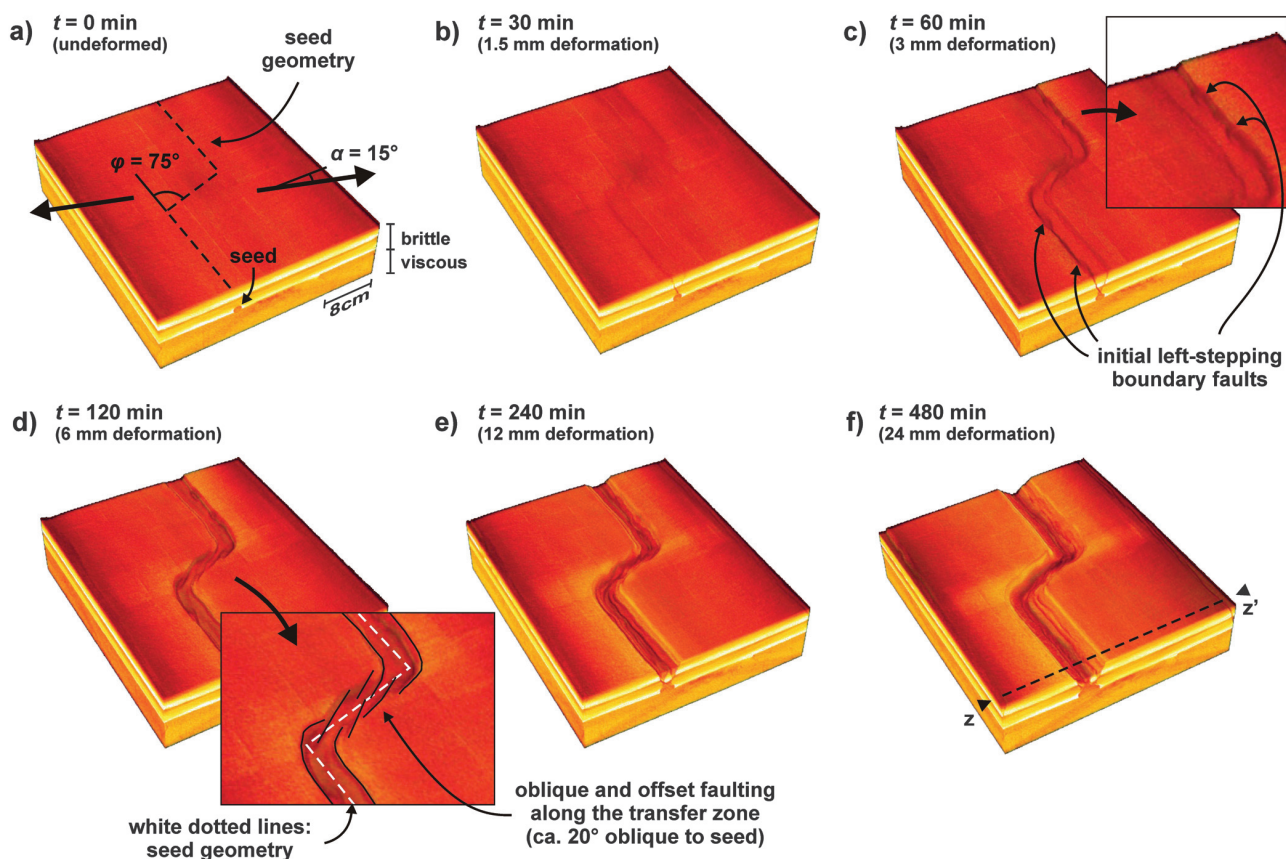
Figure 5. CT-derived images showing the 3D surface evolution of model B. (a) Initial setup: rift-connecting seed present, angle $\phi = 75°$ (underlap) and angle $\alpha = 15°$ (dextral oblique extension). (b) Faulting starts along the seeds. (c) Initial oblique boundary faults form due to oblique extension, whereas a transfer zone forms along the rift-connecting seed. (d) The transfer zone develops distinct oblique faulting. (e and f) Initial oblique boundary faults connect to form continuous boundary faults. The final transfer zone structure is slightly oblique to the original seed orientation (f). For vertical section z-z', see Figure 6.

(Figure 4h and 4n), yet CT-derived surface images and sections, allow a much more detailed structural analysis (Figures 5–7).

The first structures to appear on the 3D CT images are normal faults (initial dip angle of approximately 70°) along the main seeds (Figure 5b). These faults initially form at the side of the seed that is closest to the sidewalls creating an asymmetric graben. After approximately 60 min (3 mm of deformation), however, rift boundary faults also develop on the other side of the rift to render the rift symmetric (Figure 5c). The rift boundary faults are not completely continuous structures; initial faults are offset in a left-stepping fashion, and their surface trace strikes are approximately 8° oblique to the main rift trend (Figure 5c). However, they rapidly link up to form continuous boundary faults (Figure 5e and 5f). Within the rift segments, a secondary set of antithetic normal faults develops and a horst develops in the middle of the rift as a result (Figures 5e and 6). However, these internal structures are disrupted toward the end of the model run. Also, the seed is deformed as a result

of the rift structure above it. We observe tilted fault blocks sinking into the seed (Figures 5f and 6).

The horizontal and vertical CT sections allow a better analysis of the transfer zone area (Figure 7). In contrast to the structures along the main rift segments, the transfer zone structures are poorly developed at first. We observe combined strike-slip and oblique-slip normal faulting (initial fault dip angle approximately 90° and 76°, respectively) starting along the rift-connecting seed (Figure 7b and 7c). The vertical offset along the rift boundary faults is limited. However, the strike-slip fault within the transfer
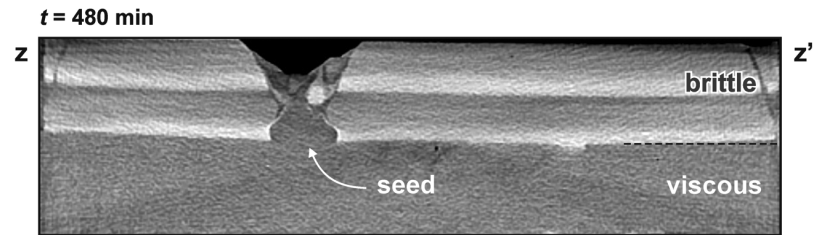
Figure 6. CT section through a main rift segment in model B, showing the rift internal structure at the end of the model run. The layering in the brittle layer is due to the density difference between the quartz and corundum sand (see Table 1). Compare with Figure 2g for the initial state. For the section location, see Figure 5.
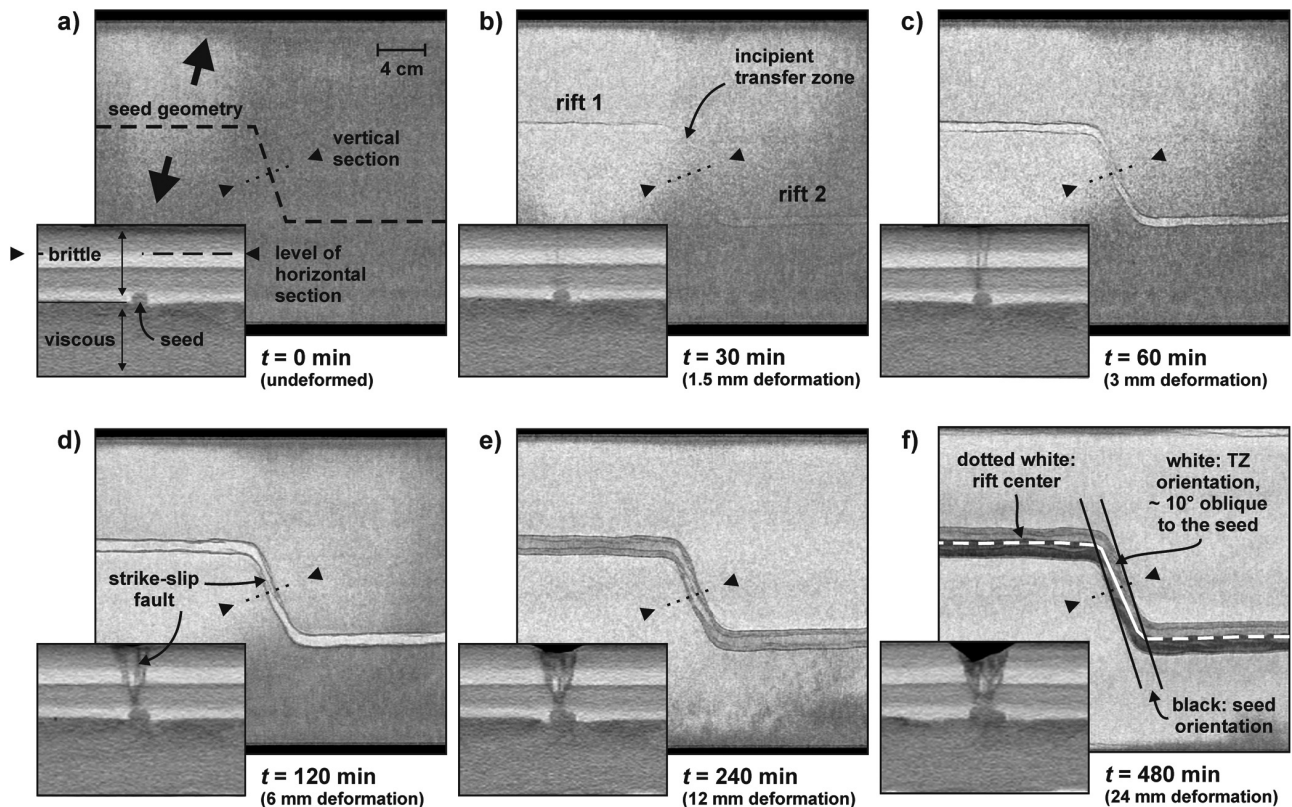
Figure 7. CT analysis of model B with horizontal and vertical sections. (a) Initial setup (rift-connecting seed present, $\phi = 75°$, $\alpha = 15°$). (b-f) Model evolution, revealing the location and nature of faulting within the model. The horizontal sections are taken approximately 2.5 cm above the brittle-ductile interface; see also the vertical section in (a). The vertical sections are perpendicular to the transfer zone; their location is indicated by a dashed line on the horizontal sections. (f) Also shown is the oblique orientation of the transfer zone with respect to the seed below it.

zone is well developed and runs from one rift segment to the other (Figure 7d–7f). Throughout the model run, the main rift basins remain wider and deeper than the basin that opens at the transfer zone. The final rift basin width is approximately 2.3 H (4.6 cm) at the main rift segments and 1.6 H (3.2 cm) within the transfer zone. Corresponding maximum basin depths amount to approximately 0.8 H (1.6 cm) and 0.4 H (0.8 cm) along the main rift segments and within the transfer zone, respectively.

Similar to the rift boundary faults along the main rift segments, the transfer zone boundary faults form along the rift-connecting seed trend, but they are offset at several places (Figure 5d). In fact, the individual faults measured at the surface tend to be oriented approximately 20° oblique to the rift-connecting seed at depth. Also, the whole transfer zone structure itself is at the surface some 10° oblique with respect to the rift-connecting seed (Figures 5d and 7f). Due to the internal strike-slip faults, the internal transfer zone structure is complex. The vertical CT sections perpendicular to the transfer zone reveal its nature as a transtensional fault zone because it combines strike-slip and normal fault features. We observe a narrow graben with steep boundary faults and vertical strike-slip faults within it (Figure 7, insets).

Results series 2
Series 2: General overview

The top view images of series 2 models, in which rift segments are underlapping and not connected by any seed, are presented in Figure 8. The characteristics of the main rift segments are similar to those in series 1, as is the rift propagation behavior. The 30° (dextral) oblique extension models in series 2 (Figure 8a–8c) develop rift segments along the seeds that propagate approximately perpendicular to the extension direction. For $\phi = 90°$ (Figure 8a), the propagating rifts curve around each other. When $\phi = 45°$ (Figure 8b), the extension direction makes the segments grow straight toward each other, forming a continuous basin. However, in the $\phi = 15°$ case (Figure 8c), the seed underlap is such that the propagation of the segment perpendicular to the extension directions almost causes them to miss each other. When extension is orthogonal (Figure 8d–8i), rift propagation is also subperpendicular to the direction of extension. Therefore, the propagating rifts do not lead to hard linkage in the $\phi = 90°$–60° cases (Figure 8d–8f). However, in the $\phi = 45°$–15° cases (Figure 8g and 8i), the rift segments show a tendency to grow toward each other, although for the $\phi = 15°$ model (Figure 8i) a full transfer zone does not develop.

A similar situation with respect to the relation between the extension direction and rift propagation direction is seen in the −30° sinistral oblique extension models. The $\phi = 90°$–45° models (Figure 8j–8l) show rift segments propagating away from each other, subperpendicular to the extension direction. However, when $\phi = 30°$ or 15° (Figure 8m and 8n), hard linkage occurs as models establish TZs. We ran multiple models with $\phi = 30°$ and $\alpha = −30°$ to examine this in further
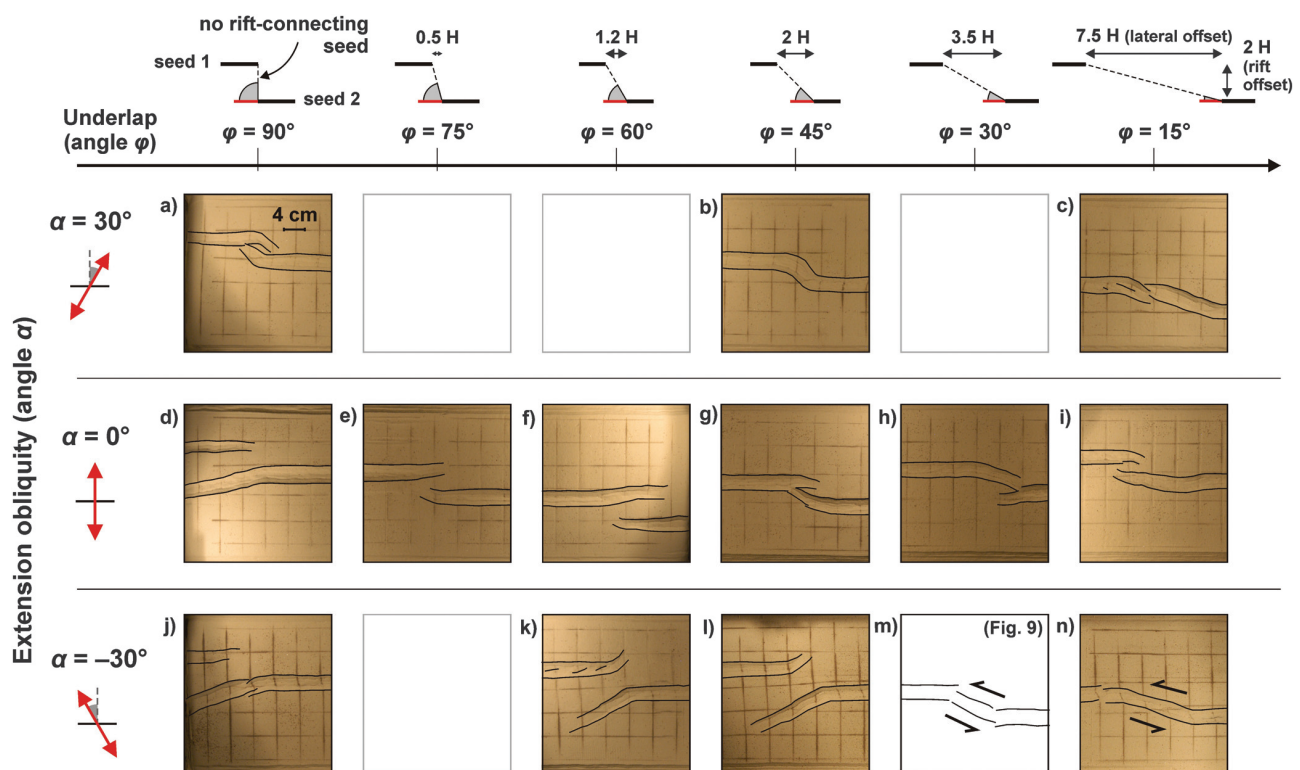
Figure 8. Top views depicting the final surface structures of 13 models from series 2 as a function of extension direction (angle α) and seed underlap (determined by angle ϕ). Faults are indicated with black lines. The black and white image (m) is shown in Figure 9.

detail, and we observed a range of characteristic features (models C–G; Figure 9). During the 480 min or 24 mm (1.2 H) of −30° (sinistral) oblique extension, models C and D develop an initial sinistral strike-slip fault zone (Figure 9b and 9f) that subsequently evolves in a transfer zone basin connecting the rift segments (Figure 9d and 9h). This final transfer zone basin is situated between continuous rift boundary faults, along which sinistral normal oblique-slip motion is accommodated. Note that model G (Figure 9q–9t) has a rift-connecting seed and technically belongs to series 1, but is shown here for comparison. It is clear that the structures follow the trace of the rift-connecting seed in model G, but the structures are very similar to those seen in models C and D.

In model E (Figure 9i–9l) on the other hand, a transfer zone is present, but it is poorly developed and it is essentially strike-slip dominated. Instead of forming a continuous basin structure as in models C and D, model E has one of the rift branches propagating away from the rift, subperpendicular to the extension direction as

seen in the other sinistral oblique extension models in series 1 and 2 (Figure 4 and 8). Model F (Figure 9m–9p), which is the CT-scanned model that will be discussed in more detail below, develops similar features as model E: one rift branch propagating away and rift linkage through a sinistral strike-slip-dominated transfer zone.

Note that the characteristics of the strike-slip transfer zone structures in the model E and F examples (Figure 9l and 9p) resemble the early stages of the transfer zone structures in models C, D, and G (Figure 9b, 9f, and 9r). But, although deformation is fully accommodated by a transfer zone evolving into a continuous trough in models C, D, and G, part of the deformation in models E and F goes into the propagating rift branches. Therefore, the TZs remain shallow and strike-slip dominates in the latter models.

Series 2: CT-scanned model (model F)

To further assess the phenomenon of rift connection by a strike-slip transfer zone during sinistral oblique extension, we ran a $\alpha = -30°$, $\phi = 30°$ model with double
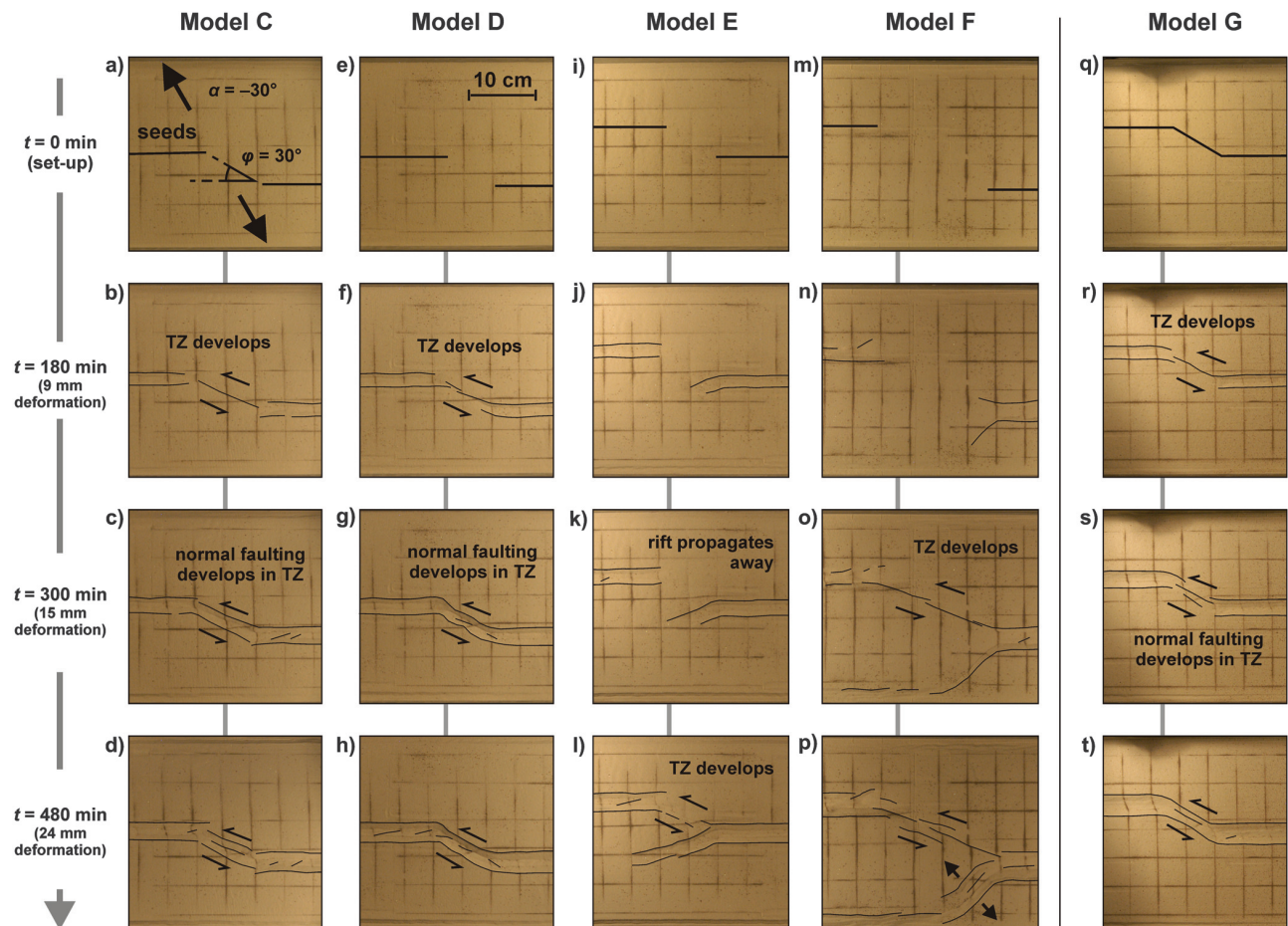
Figure 9. Surface structure evolution of five models with $\phi = 30°$ and $\alpha = -30°$ to assess the development of sinistral strike-slip transfer zones (TZs). Models C (a-d), D (e-h), E (i-l), and G (q-t) have a normal layer thickness (a 2 cm ductile and a 2 cm brittle layer). The CT-scanned model F (m-p, see also Figures 10–13) has the same basic setup but a double layer thickness and therefore a larger seed offset. Note that model G (q-t) has a rift-connecting seed, and technically belongs to series 1. However, it is included here for comparison. Faults are indicated with black lines.

layer thickness as well as double rift offset and without rift-connecting seed in the CT scanner (model F). The CT data are used to create 3D surface images (Figure 10) and horizontal and vertical sections (Figure 11) that allow more detailed analysis. The model generates two rift segments, of which one propagates subperpendicular to the extension direction and a strike-slip-dominated transfer zone between the two rift segments.

In model F, deformation initially takes place along the seeds (Figure 10b). Both rift segments show a tendency to propagate perpendicular to the extension direction. However, at $t = 120$ min (6 mm of deformation), vertical sinistral strike-slip fault segments start developing between the main rifts (Figure 11b). Some 30 min later, these fault segments form a zone of en echelon strike-slip faults, all oriented 20° oblique to the rift trend in a Riedel fault configuration (Figures 10c and 11c). As deformation progresses, oblique-slip normal faulting becomes more prominent and a negative flower structure develops (sections in Figure 11c–11f). The associated horizontal sections also show how the Riedel faults connect in various orientations.

Meanwhile, the main rift basins continue developing above the seeds and one rift segment propagates toward the side of the model. This propagating rift arm is perhaps partially a boundary effect as its orientation

is not perpendicular with respect to the extension direction (compare with model E; Figure 9i–9l). The rift branch takes up a large portion of deformation so that the strike-slip dominated transfer zone only accommodates a total of 0.6 cm (0.15 H) sinistral strike-slip motion. Subsidence along the transfer zone is also limited (approximately 1 mm or 0.025 H).

Discussion

Characteristics of the main rift segments

The geometry and evolution of the rift segments away from the rift interaction zones in our models are similar to those observed and described by Zwaan et al. (2016). In general, an increase in extension obliquity (angle α) results in a decrease in graben width and depth as the system becomes less extension dominated. Higher degrees of extension obliquity also result in more features such as en echelon boundary faults and rift-internal oblique structures. The main rift segments propagate roughly perpendicular to the extension direction as previously observed in modeling studies involving oblique extension (Tron and Brun, 1991; McClay and White, 1995; McClay et al., 2002) and in natural settings (Dauteuil and Brun, 1993; Morley et al., 2004). Our models produce relatively narrow structures with minimal internal details compared with those in previous modeling
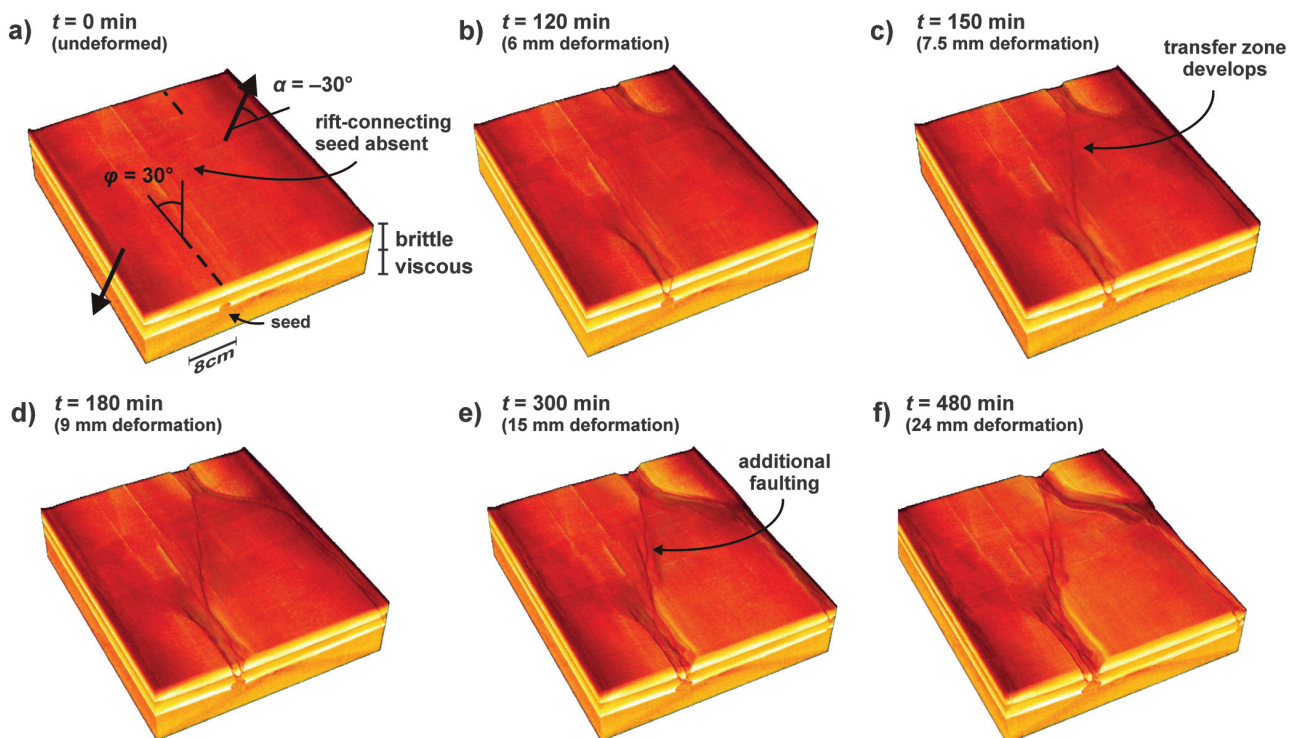
Figure 10. CT-derived images showing the 3D surface evolution of model F. (a) Initial setup: rift-connecting seed absent, angle $\phi = 30°$ (underlap) and angle $\alpha = -30°$ (sinistral oblique extension). (b) Faulting initiates along the seeds. (c) A strike-slip transfer zone appears and on the rift arm it propagates toward the model edge. (d-f) The established structures evolve further: As the rift segments and rift branch grow larger, the transfer zone develops more expressed strike-slip faults. (f) Shows, in addition, the orientation of the transfer zone with respect to the rift-connecting seed below.

studies and some natural examples, but this is quite permissible because here we focus rather on rift interaction processes on a regional scale than on detailed internal rift geometries.

Rift segment propagation and interaction

The models from series 1 and 2 show the extension direction as a dominant factor controlling the propagation direction of rift segments because rift propagation tends to be subperpendicular to it. As a consequence, we observe that the rift linkage of right-stepping rift segments is generally promoted by dextral oblique extension that causes the rifts to propagate toward each other and prevented by sinistral oblique extension that has them grow apart. However, in a mirrored system with rift segments arranged in a left-stepping fashion, dextral and sinistral oblique extension switch places (see also Figure 13). Dextral oblique extension now should prevent rift linkage because rift segments grow apart under these conditions. In contrast, sinistral oblique extension should cause left-stepping rift segments to connect. Rift segment arrangement is therefore a second important influence on rift interaction, and rift linkage is most likely when the extension direction is

such that rift segment propagation is directed toward the other rift segment. Note that the orthogonal extension models from series 2 do not fully fit the general picture. The rift segments in the larger underlap models ($\phi = 45°$ and 30°; Figure 8g and 8h) do partially connect. Possibly the 2 H offset between the rifts is not large enough to prevent them from interacting after all, or rift propagation directions can vary up to a certain degree in our specific setup.

Similar influences of oblique extension on fault orientation and associated rift propagation directions are reported in previous analog models (Hus et al., 2005; Zwaan et al., 2016), although sinistral oblique extension was not tested before. The curving of propagating rifts toward each other under orthogonal extension when $\phi = 90°$ or higher isolates part of the model between both propagating rift segments, a so-called rift pass (Nelson et al., 1992), which is also observed in previous analog models and can lead to microcontinent formation (Müller et al., 2001; Tentler and Acocella, 2010). We can expect for our specific setup that dextral oblique extension enhances this process because it induces rifts to propagate toward each other, especially when rifts are too far apart to interact under orthogonal extension conditions.
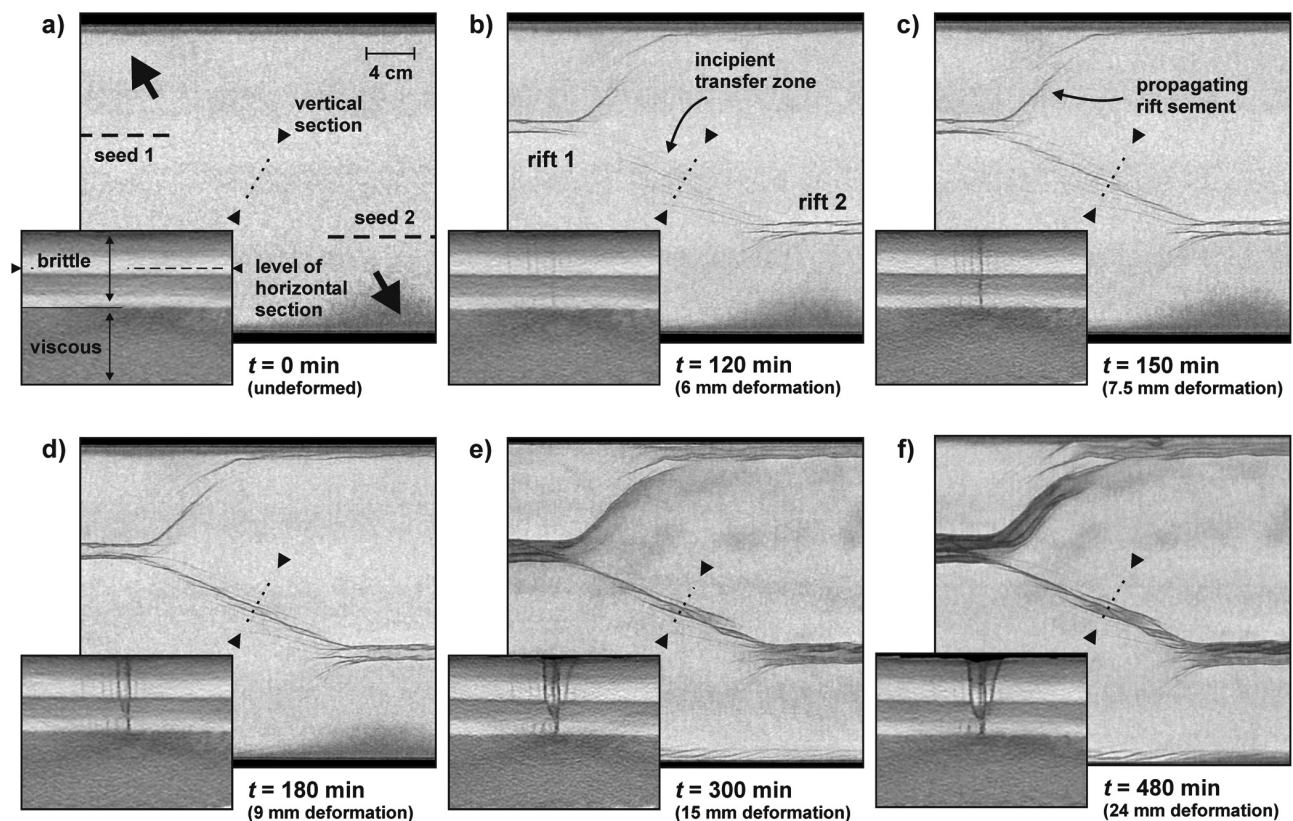
Figure 11. CT analysis of model F with horizontal and vertical sections. (a) Initial setup (rift-connecting seed absent, $\phi = 30°$, $\alpha = -30°$) and (b-f) model evolution, revealing the location and nature of faulting within the model. The horizontal sections are taken approximately 2.5 cm above the brittle-ductile interface; see also the vertical section in (a). The vertical sections are perpendicular to the transfer zone; their location is shown by a dashed line on the horizontal sections.

Rift-connecting seeds and rift segment interaction

Our models show limited reactivation of secondary pre-existing weaknesses. The secondary seeds only activate when they are oriented favorably to the regional tectonic stresses. Furthermore, in our experiments, rift segments in models with angle $\phi = 90°$ under orthogonal extension fail to link. This is in contrast with previous models (Acocella et al., 1999; Dauteuil et al., 2002), but it is in accordance with other models such as those completed by Le Calvez and Vendeville (2002), illustrating a fundamental difference between traditional rigid baseplate setups, which force deformation along the plate boundaries, and setups that allow more freedom for the model to evolve.

The notion that inherited structures do not necessarily reactivate has been previously explored, for example, in models run by Nalpas et al. (1995), although their study was aimed at initial rifting and subsequent inversion. Note that model series 2 does not cover the whole spectrum of model series 1 and only focuses on the underlap models since we expect the equivalent overlap models in series 2 to have the same characteristics as those in series 1. This is illustrated by the $\phi = 90°$ models from series 1 and 2 that produce very similar structures (compare Figure 4c, 4i, and 4o with Figure 8a, 8d, and 8j). However, inherited structures might influence structures in ways that our model setup does not capture, such as creating boundaries for propagating rifts, causing general weakening of the brittle crust, and locally changing the state of stress (Bell, 1996; Morley, 2010).

Transfer zone details

Strain partitioning accounts for the limited strike-slip faulting that occurs at the tip of rift segments in some models (Figure 4o, 4s, 4u, and 4v) as also observed in models by Zwaan et al. (2016). Moreover, strain partitioning can also produce a major strike-slip fault within a transfer zone that runs from one rift segment to the other as seen in model B (with 15° oblique extension; Figure 7). This is similar to observations in orthogonal extension models by Acocella et al. (1999), as is the fact that the whole transfer zone itself might form oblique to the deeper crustal weakness. In previous studies, the surface orientation of transfer zones is expressed with angle ϕ (Acocella et al., 1999; Corti, 2012), but because this is also used to describe the orientation of structural inheritance, we propose to use angle κ (Greek kappa) for the orientation of the transfer zone instead (Figure 12).

Rift segment linkage under sinistral oblique extension conditions

The sinistral oblique extension models ($\alpha = -30°$) of series 2 show the expected rift propagation behavior as a function of extension direction that also occurs in series 1 (Figures 4a–4f and 8a–8l), except for the $\phi = 30°$ and 15° models (Figures 8m, 8n, and 9). These develop a spectrum of TZs between the main rift segments, ranging from a rift structure with a sinistral strike-slip component along the boundary faults (models C and D; Figure 9a–9h) to a more discrete sinistral strike-slip zone along with one rift branch propagating away from the rift (models E and F; Figure 9i–9p). Although the rift branch orientation in model F is slightly off (not perpendicular to the extension direction), probably due to the influence of faulting at the model edge, it does fit in the general picture. In a way, these different models can be seen as different stages when only the transfer zone evolution is concerned. The strike-slip-dominated TZs in models E and F (Figure 9i–9p) then represent the early stages of transfer zone development. In these models, the propagating rift branches take up a part of the deformation resulting in a less evolved transfer zone. In models C and D (Figure 9a–9h), all deformation is accommodated by the transfer zone alone. This concentration of deformation results in basin formation following the initial strike-slip phase that is also captured by models E and F. The final results of models C and D thus illustrate a more advanced stage in transfer zone development.

Our four $\phi = -30°$, $\alpha = -30°$ models (models C–F) without a rift-connecting seed all establish a transfer zone between the main rift segments. However, some models (E and F; Figure 9i–9p) develop an additional propagating rift branch similar to those in (most) other $\alpha = -30°$ models (Figure 8j–8l). These hybrid features in models E and F indicate that the $\alpha = -30°$, $\phi = 30°$ situation marks a transition between two modes of rift interaction. When $\phi > 30°$, we should expect accommodation zones to form and rifts to grow apart, which is consistent with our models (Figure 8j–8l), whereas $\phi \leq 30°$ settings will produce strike-slip-dominated TZs, as is confirmed by our $\phi = 15°$ model (Figure 8n). When we then add a rift-connecting seed as in model G (Figure 9q–9t), we observe the exact same structures as in the models without a rift-connecting seed, i.e., models C and D (Figure 9a–9h). The transfer zone in model G does follow the trend of the rift-connecting seed, but it is not clear from our models whether the seed is really activated or whether it just has the same orientation as the transfer zone. However, the fact that model G does not develop any propagating rift branches such as those in models C and D could indicate a localizing effect of the seed, and the absence of a seed could allow the system the freedom to develop propagating rift branches. Our model results thus do not exclude any influence of basement structures on transfer zone formation, but they show that such structures are not strictly necessary to produce rift linkage through a strike-slip-dominated transfer zone.

The formation of strike-slip TZs in the $\phi \leq 30°$, $\alpha = -30°$ models (structures schematically depicted in Figure 12a) indicates strong local changes in the regional stress field (Figure 12b). Throughout the model, sinistral oblique extension causes a state of stress with σ_1 vertical to the surface and σ_3 oriented horizontally, roughly parallel to the direction of extension ("oblique extension" setting; Figure 12b). As the seeds localize deformation and normal faults strike perpendicular to σ_3,

this state of stress causes initial oblique faulting along the seeds. When the initial rift segments start propagating away from the seeds, the developing rift branch, free from the localizing influence of the seed, directs itself perpendicular to the regional σ_3. The rift segments should thus simply grow apart, but we observe the formation of strike-slip TZs (Figure 12a). To create a strike-slip fault zone between the rift segments, σ_1 and σ_3 must be reoriented so that they lie within a horizontal plane, some 30° and 60° oblique to the strike-slip zone, respectively. Thus, the local σ_1 is now oriented approximately 25° oblique with respect to the regional σ_2 and the local σ_2 replaces the regional σ_1 as the vertical principal stress ("local strike slip," Figure 12b). Such local stress changes also occur at stepovers in strike-slip fault systems (Okubo and Schultz, 2006; De Paola et al., 2007). The TZs in our models do resemble releasing bends observed in such settings, yet the kinematics do not fit since releasing bends form in a dextral slip environment (for a right-stepping fault segment arrangement, McClay and Bonora, 2001), whereas our models involve sinistral slip.

We suggest that the local change in the state of stress in our $\phi \leq 30°$ models is related to the absence of a seed in the large space between the two underlapping rift segments (Figures 8m, 8n, and 9). Models with less space between the underlapping rift segments ($\phi > 30°$) do not form strike-slip TZs (Figure 8j–8l). The second factor involved in the formation of a strike-slip fault zone is the occurrence of sinistral deformation along the rift segments. This motion causes a transfer of material toward the rift interaction zone (Figure 12a). Without a seed to localize extensional deformation, and with material being forced into the rift interaction zone, the development of a strike-slip fault zone between the rift segments probably provides the most efficient way to accommodate deformation.

Comparison with natural examples

The early stages of the models from series 1 with angle ϕ of 60° or 75° and 0°–30° extension obliquity produce similar structures to the RBTZ (Figures 1a, 4g, 4h, 4m, 4n, and 5–7). As in the natural example, the secondary structural grain is reactivated (Ustaszewski et al., 2005), which is well visible in the CT scanned model B (Figures 5–7) and we observe two rift segments analogous to the Rhine Graben and the Bresse Graben with a transfer zone in between (Figure 1a). The normal component of the modeled transfer zone border faults is in agreement with an interpretation of the RBTZ being an extension-dominated

feature with minor strike-slip motion (Madritsch et al., 2009). The rift segment widths of some 2 H in the model translate to some 30–40 km in nature, which is similar to the dimensions of the natural example. The modeled transfer zone in between the rift segments remains shallow and contains limited internal oblique faulting with respect to the main rift segments (Figure 5b and 5c).

The SDR within the Rio Grande Rift (Figure 1b) represents possibly a more advanced stadium of a similar system as the RBTZ, with near-orthogonal regional extension (Minor et al., 2013). It also accommodates sinistral motion and forms a continuous sediment-filled basin system comparable with the transfer zone that follows the secondary seed in model B (Figure 5d–5f). An alternative interpretation involves sinistral oblique extension on a region scale (Chapin and Cather, 1994), which would qualify our sinistral oblique extension models for comparison. The structures in models C, D, and G (Figure 9a–9h and 9q–9t) bear a resemblance to the SDR. We observe a continuous basin within the transfer zone with sinistral oblique-slip motion. However, the orientation of the the transfer zone is slightly different: Angle κ is 25° in the models against 45° in nature. This might indicate some influence of the structural inheritance present in the natural example.
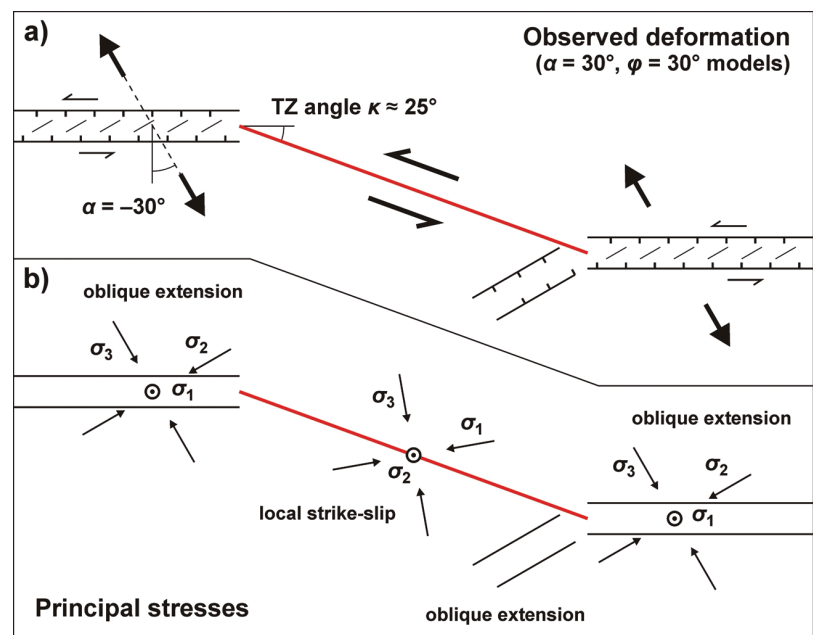
Figure 12. Schematic overview of (a) observed deformation structures at the model surface and (b) inferred principal stresses at the time of transfer zone formation within our $\phi = 30°$ models with −30° (sinistral) oblique extension. The regional state of stress, present along the rift segments and any propagating rift branch, has σ_1 vertical and σ_3 horizontal in the −30° sinistral oblique extension direction. The strike-slip character of the transfer zone indicates a local change in stress: σ_1 and σ_3 become horizontal (approximately 30° and 60° oblique to the transfer zone, respectively) and oblique to the transfer zone, whereas σ_2 is now vertical.

Tanganyika-Rukwa-Malawi fault zone

The strike-slip TZs observed in the sinistral oblique extension models from series 2 bear resemblance to the situation in East Africa according to the "oblique-opening model" put forward by Chorowicz (2005). Within the Western Branch of the East African Rift System lies the Tanganyika-Rukwa-Malawi (TRM) fault zone (Rosendahl et al., 1992; Chorowicz, 2005), an overall dextral strike-slip zone that connects the left-stepping rift branches currently in a dextral oblique extension system with $\alpha = -30°$ (Saria et al., 2014; Figures 1c, 1d, and 13). When we compare this natural example with model F, mirrored to mimic this natural example, there are more similarities: The strike-slip zone is oriented at a low angle ($\kappa = 20°–25°$) to the rift segment orientation in the model and in nature. Also, the Tanganyika part of the TRM fault zone seems to propagate slightly away from the Malawi rift, as we observe with one rift segment in our model F (Figure 13). However, the latter is (partially) a boundary effect due to the normal faulting at the model edge.

Our $\phi = 30°$, $\alpha = -30°$ models thus seem to fit the natural example, but the interpretation of the TRM fault zone as a dextral strike-slip zone is challenged by an orthogonal opening model, in which all rift basins form due to extension perpendicular to the rift trends (Morley, 2010; Delvaux et al., 2012). Field evidence indicates that the steep rift boundary faults of the Rukwa Basin are indeed rather normal or dip-slip faults instead of strike-slip faults. Their apparent strike-slip character is proposed to derive from an earlier phase of strike-slip tectonics in the early Mesozoic after which they were reactivated during late Cenozoic NE-SW extension in the area. Yet our $\alpha = -30°$, $\phi = 30°$, models without propagating rift branches do clearly develop initial strike-slip fault zones that evolve into graben-like struc-

tures toward the end of the model run (models C, D, and G; Figure 9a–9d, 9f–9h, and 9q–9t). It would thus be possible to fit the field observations in the oblique-opening model, although the dip-slip-dominated boundary faults along the Rukwa Basin do not fully correspond with the significant strike-slip character of our modeled TZs.

The reason for this could be the absence of crustal strength variations in our models as analog modeling and field studies have pointed out that these can cause local changes in the extension direction (Morley, 2010; Corti et al., 2013; Philippon et al., 2015). Michon and Sokoutis (2005) suggest that such processes influence the TRM fault zone because it is situated in a mobile orogenic belt along the Tanzania Craton (Figure 13). The fact that our modeled TZs and the Rukwa Basin do not fully correlate could thus be due to the absence of such crustal strength variations in our model setup, preventing a full reconstruction of the TRM fault zone characteristics.

Conclusion

Our models examining the effects of oblique extension and structural inheritance on rift interaction lead to the following conclusions:

1) Extension direction is a key influence on rift linkage; right-stepping rift segments are more likely to connect with dextral oblique extension because they tend to grow and propagate toward each other. This mechanism could promote microcontinent formation. In contrast, orthogonal extension and sinistral oblique extension generally do not result in rift linkage because the right-stepping rift segments propagate in a parallel fashion or grow apart, respectively.

2) Although sinistral oblique extension generally prevents rift linkage between right-stepping rift segments, it can lead to linkage in the shape of a strike-slip-dominated transfer zone when the rift segments are laterally far apart.

3) The previous two points are also valid for a mirrored system; left-stepping rift segments form TZs as sinistral oblique extension makes the rift segments propagate toward each other. In contrast, orthogonal and dextral oblique-extension result in parallel rift propagation or rifts growing apart, respectively, preventing transfer zone formation. Underlapping left-stepping rift segments can form a strike-slip transfer zone under dextral extension conditions.

4) Secondary structural inheritance might influence rift linkage, but only when the extension direction is favorable for reactivation. Otherwise, propagating rifts will simply align approximately perpendicular to the extension direction.
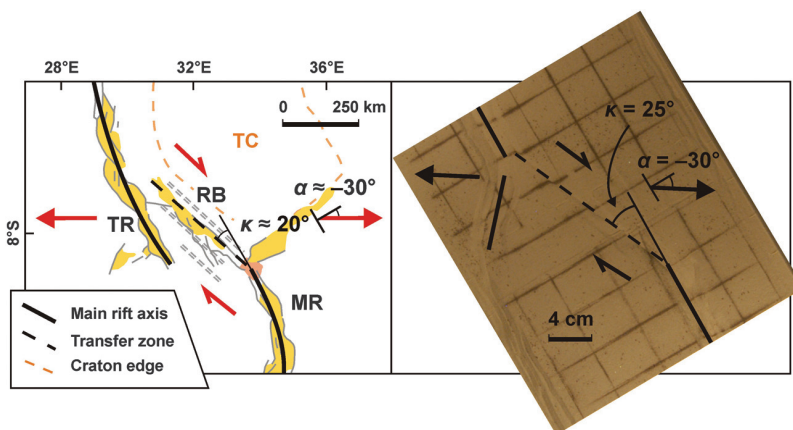
Figure 13. Comparison between (left) the Tanganyika-Rukwa-Malawi fault zone and (right) a final top view of model F. Note that the model image is mirrored to fit the natural example. We observe (1) a similar extension direction (angle α), (2) a strike-slip transfer zone with the same motion with (3) a similar orientation to the main rifts (angle κ), and (4) rift segments that grow apart. MR = Malawi Rift, RB = Rukwa Basin, TR = Tanganyika Rift, and TC = Tanzania Craton. Image modified after Ebinger (1989), Acocella et al. (1999), Corti et al. (2007), and Saria et al. (2014). For the location, see Figure 1c.

5) When secondary structural inheritances are reactivated, the resulting transfer zone and internal faults commonly follow their general orientation. Mild obliquity does occur as these structures attempt to align perpendicular to the extension direction.

6) Several of the characteristic structures we observe in our models are also present in natural rift settings, such as the Rhine-Bresse Transfer Zone, the Rio Grande Rift, and the East African Rift System.

Acknowledgments

Appendix A

Effect of lower extension velocity

High brittle-ductile coupling due to high strain rates or high viscosities in the ductile domain causes distributed deformation (wide rifting) in the brittle parts of the crust (Brun, 1999; Buiter et al., 2008), preventing the development of discrete fault zones (Allken et al., 2011; 2012; Zwaan et al., 2016). It is thus necessary to decrease deformation rates in our analog models in order to limit wide rifting effects, as shown in Figure A-1.

References

Acocella, V., C. Faccenna, R. Funiciello, and F. Rossetti, 1999, Sand-box modeling of basement-controlled transfer zones in extensional domains: Terra Nova, **11**, 149–156, doi: 10.1046/j.1365-3121.1999.00238.x.

Acocella, V., P. Morvillo, and R. Funiciello, 2005, What controls relay ramps and transfer faults within rift zones? Insights from analogue models: Journal of Structural Geology, **27**, 397–408, doi: 10.1016/j.jsg.2004.11.006.

Aldrich, M. J., 1986, Tectonics of the Jemez mountains and Rio Grande rift: Journal of Geophysical Research, **91**, 1753–1762, doi: 10.1029/JB091iB02p01753.

Allemand, P., and J.-P. Brun, 1991, Width of continental rifts and rheological layering of the lithosphere: Tectonophysics, **188**, 63–69, doi: 10.1016/0040-1951(91)90314-I.

Allken, V., R. S. Huismans, and C. Thieulot, 2011, Three-dimensional numerical modeling of upper crustal extensional systems: Journal of Geophysical Research, **116**, B10409, doi: 10.1029/2011JB008319.

Allken, V., R. S. Huismans, and C. Thieulot, 2012, Factors controlling the mode of rift interaction in brittle-ductile coupled systems: A 3D numerical study: Geochemistry, Geophysics, Geosystems, **13**, Q05010, doi: 10.1029/2012GC004077.

Basile, C., and J.-P. Brun, 1999, Transtensional faulting patterns ranging from pull-apart basins to transform continental margins: An experimental investigation: Journal
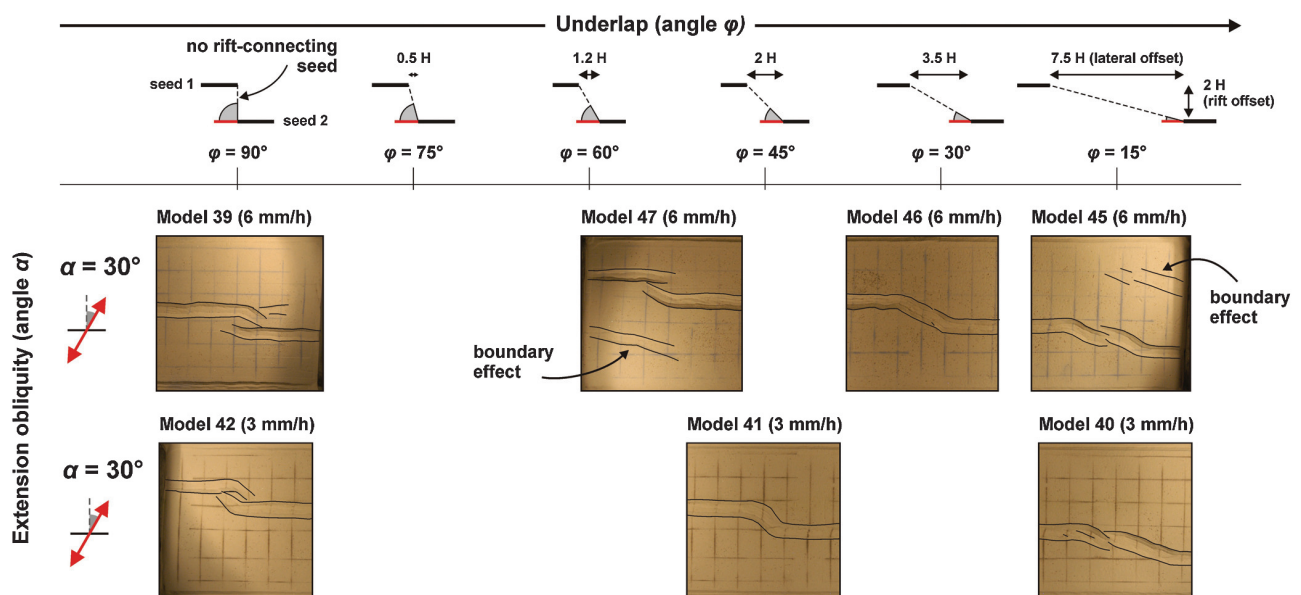
Figure A-1. Velocity comparison, depicting how lowering extension velocity from 6 mm/h as applied by Zwaan et al. (2016) to 3 mm/h in this study decreases boundary effects, i.e., additional faulting, without hindering the development of the main rift structures.

of Structural Geology, **21**, 23–37, doi: 10.1016/S0191-8141 (98)00094-7.

Bell, J. S., 1996, In situ stresses in sedimentary rocks (Part 2): Applications of stress measurements: Geoscience Canada, **23**, 135–153.

Bennett, S. E. K., and M. E. Oskin, 2014, Oblique rifting ruptures continents: Example from the Gulf of California shear zone: Geology, **42**, 215–218, doi: 10.1130/G34904.1.

Brun, J.-P., 1999, Narrow rifts versus wide rifts: Inferences for the mechanics of rifting from laboratory experiments: Philosophical Transactions of the Royal Society of London A, **357**, 695–712, doi: 10.1098/rsta .1999.0349.

Brune, S., 2014, Evolution of stress and fault patterns in oblique rift systems: 3-D numerical lithospheric-scale experiments from rift to breakup: Geochemistry, Geophysics, Geosystems, **15**, 3392–3415, doi: 10.1002/ 2014GC005446.

Brune, S., A. A. Popov, and S. V. Sobolev, 2012, Modeling suggests that oblique extension facilitates rifting and continental break-up: Journal of Geophysical Research, **117**, B08492, doi: 10.1029/2011JB008860.

Buck, W. R., 1991, Modes of continental lithospheric extension: Journal of Geophysical Research, **96**, 161–178, doi: 10.1029/91JB01485.

Buiter, S. J. H., R. S. Huismans, and C. Beaumont, 2008, Dissipation analysis as a guide to mode selection during crustal extension and implications for the styles of sedimentary basins: Journal of Geophysical Research, **113**, B06406, doi: 10.1029/2007JB005272.

Chapin, C. E., and S. M. Cather, 1994, Tectonic setting of the axial basins of the northern and central Rio Grande rift, *in* G. R. Keller, and S. M. Cather, eds., Basins of the Rio Grande rift: Structure, stratigraphy, and tectonic setting: Geological Society of America, 5–25, doi: 10 .1130/SPE291-p5.

Childs, C., J. Watterson, and J. J. Walsh, 1995, Fault overlap zones within developing normal fault systems: Journal of the Geological Society, **152**, 535–549, doi: 10.1144/ gsjgs.152.3.0535.

Chorowicz, J., 2005, The East African rift system: Journal of African Earth Sciences, **43**, 379–410, doi: 10.1016/j. jafrearsci.2005.07.019.

Clifton, A. E., and R. W. Schlische, 2001, Nucleation, growth and linkage of faults in oblique rift zones: Results from experimental clay models and implications for maximum fault size: Geology, **29**, 455–458, doi: 10.1130/0091-7613 (2001)029<0455:NGALOF>2.0.CO;2.

Corti, G., 2012, Evolution and characteristics of continental rifting: Analog modeling-inspired view and comparison with examples from the East African Rift System: Tectonophysics, **522–523**, 1–33, doi: 10.1016/j.tecto.2011.06 .010.

Corti, G., M. Bonini, D. Sokoutis, F. Innocenti, P. Manetti, S. Cloetingh, and G. Mulugeta, 2004, Continental rift architecture and patterns of magma migration: A dynamic

analysis based on centrifuge models: Tectonics, **23**, TC2012, doi: 10.1029/2003TC001561.

Corti, G., M. Philippon, F. Sani, D. Keir, and T. Kidane, 2013, Re-orientation of the extension direction and pure extensional faulting at oblique rift margins: Comparison between the Main Ethiopian Rift and laboratory experiments: Terra Nova, **0**, 1–9, doi: 10.1111/ter .12049.

Corti, G., J. van Wijk, S. Cloetingh, and C. K. Morley, 2007, Tectonic inheritance and continental rift architecture: Numerical and analogue models of the East African Rift system: Tectonics, **26**, TC6006, doi: 10.1029/ 2006TC002086.

Dauteuil, O., O. Bourgeois, and T. Mauduit, 2002, Lithosphere strength controls oceanic transform zone structure: Insights from analogue models: Geophysical Journal International, **150**, 706–714, doi: 10.1046/j.1365-246X .2002.01736.x.

Dauteuil, O., and J.-P. Brun, 1993, Oblique rifting in a slow-spreading ridge: Nature, **361**, 145–148, doi: 10.1038/ 361145a0.

Delvaux, D., F. Kervyn, A. S. Macheyeki, and E. B. Temu, 2012, Geodynamic significance of the TRM segment in the East African Rift (W-Tanzania): Active tectonics and paleostress in the Ufipa plateau and Rukwa basin: Journal of Structural Geology, **37**, 161–180, doi: 10.1016/j.jsg .2012.01.008.

De Paola, N., R. E. Woldsworth, C. Collettini, K. J. W. Mccaffrey, and M. R. Barchi, 2007, The structural evolution of dilational stepovers in regional transtensional zones: Geological Society of London, Special Publications, **290**, 433–445, doi: 10.1144/SP190.17.

Ebinger, C. J., 1989, Tectonic development of the western branch of the East African rift system: Geological Society of America Bulletin, **101**, 885–903, doi: 10.1130/ 0016-7606(1989)101<0885:TDOTWB>2.3.CO;2.

Elmohandes, S.-E., 1981, The central European graben system: Rifting imitated by clay modeling: Tectonophysics, **73**, 69–78, doi: 10.1016/0040-1951(81)90174-8.

Faulds, J. E., and R. J. Varga, 1998, The role of accommodation zones and transfer zones in the regional segmentation of extended terranes, *in* J. E. Faulds, and J. H. Stewart, eds., Accommodation zones and transfer zones: The regional segmentation of the basin and range province: Geological Society of America Special Paper, 1–46, doi: 10.1130/0-8137-2323-X.1.

Fossen, H., R. A. Schultz, E. Rundhovde, A. Rotevatn, and S. J. Buckley, 2010, Fault linkage and graben stepovers in the Canyonlands (Utah) and the North Sea Viking Graben, with implications for hydrocarbon migration and accumulation: AAPG Bulletin, **94**, 597–613, doi: 10.1306/10130909088.

Hubbert, M. K., 1937, Theory of scaled models as applied to the study of geological structures: Geological Society of America Bulletin, **48**, 1459–1520, doi: 10.1130/ GSAB-48-1459.

Hus, R., V. Acocella, R. Funiciello, and M. De Batist, 2005, Sandbox models of relay ramp structure and evolution: Journal of Structural Geology, **27**, 459–473, doi: 10.1016/j.jsg.2004.09.004.

Illies, J. H., 1977, Ancient and recent rifting in the Rhine-graben, *in* R. T. C. Frost, and A. J. Dikkers, eds., Fault tectonics in N.W. Europe: Geologie en Mijnbouw, 329–350.

Larsen, P.-H., 1988, Relay structures in a lower Permian basement-involved extension system, East Greenland: Journal of Structural Geology, **10**, 3–8, doi: 10.1016/0191-8141(88)90122-8.

Le Calvez, J. H., and B. C. Vendeville, 2002, Experimental designs to model along-strike fault interaction: Journal of the Virtual Explorer, **7**, 1–17, doi: 10.3809/jvirtex.2002.00043.

Madritsch, H., A. Kounov, S. M. Schmid, and O. Fabbri, 2009, Multiple fault reactivations within the intra-continental Rhine-Bresse Transfer Zone (La Serre Horst, eastern France): Tectonophysics, **471**, 297–318, doi: 10.1016/j.tecto.2009.02.044.

McClay, K., and M. Bonora, 2001, Analog models of restraining stepovers in strike-slip fault systems: AAPG Bulletin, **85**, 233–260, doi: 10.1306/8626C7AD-173B-11D7-8645000102C1865D.

McClay, K. R., T. P. Dooley, P. Whitehouse, and M. Mills, 2002, 4D-evolution of rift systems: Insights from scaled physical models: AAPG Bulletin, **86**, 935–959, doi: 10.1306/61EEDBF2-173E-11D7-8645000102C1865D.

McClay, K. R., and M. J. White, 1995, Analogue modeling of orthogonal and oblique rifting: Marine and Petroleum Geology, **12**, 137–151, doi: 10.1016/0264-8172(95)92835-K.

Michon, L., and D. Sokoutis, 2005, Interaction between structural inheritance and extension direction during graben and depocentre formation: An experimental approach: Tectonophysics, **409**, 125–146, doi: 10.1016/j.tecto.2005.08.020.

Minor, S. A., M. R. Hudson, J. S. Caine, and R. A. Thompson, 2013, Oblique transfer of extensional strain between basins of the middle Rio Grande rift, New Mexico: Fault kinematic and paleostress constraints, *in* M. R. Hudson, and V. J. S. Grauch, eds., New perspectives on Rio Grande rift basins: From tectonics to groundwater: Geological Society of America Special Paper, 345–382, doi: 10.1130/2013.2494(14).

Morley, C. K., 1999, How successful are analogue models in addressing the influence of pre-existing fabrics on rift structure?: Journal of Structural Geology, **21**, 1267–1274, doi: 10.1016/S0191-8141(99)00075-9.

Morley, C. K., 2010, Stress re-orientation along zones of weak fabrics in rifts: An explanation for pure extension in 'oblique' rift segments: Earth and Planetary Science Letters, **297**, 667–673, doi: 10.1016/j.epsl.2010.07.022.

Morley, C. K., C. Haranya, W. Phoosongsee, S. Pongwapee, A. Kornsawan, and N. Wonganan, 2004, Activation of rift oblique and rift parallel pre-existing fabrics during extension and their effect on deformation style: Examples from the rifts of Thailand: Journal of Structural Geology, **26**, 1803–1829, doi: 10.1016/j.jsg.2004.02.014.

Morley, C. K., R. A. Nelson, T. L. Patton, and S. G. Munn, 1990, Transfer zones in the East African Rift system and their relevance to hydrocarbon exploration in rifts: AAPG Bulletin, **74**, 1234–1253, doi: 10.1306%2F0C9B2475-1710-11D7-8645000102C1865D.

Müller, R. D., C. Gaina, W. R. Roest, and D. L. Hansen, 2001, A recipe for microcontinent formation: Geology, **29**, 203–206, doi: 10.1130/0091-7613(2001)029<0203:ARFMF>2.0.CO;2.

Mulugeta, G., 1988, Squeeze box in the centrifuge: Tectonophysics, **148**, 323–335, doi: 10.1016/0040-1951(88)90139-4.

Nalpas, T., S. Le Douaran, J.-P. Brun, P. Unternehr, and J.-P. Richert, 1995, Inversion of the Broad Fourteens Basin (offshore Netherlands): A small-scale model investigation: Sedimentary Geology, **95**, 237–250, doi: 10.1016/0037-0738(94)00113-9.

Naylor, M. A., J. M. Larroque, and B. D. M. Gauthier, 1994, Understanding extensional tectonics: Insights from sandbox models, *in* F. Roure, N. Ellouz, V. S. Shein, and I. Skvortsov, eds., Geodynamic evolution of sedimentary basins: Éditions Technip, 69–83.

Nelson, R. A., T. L. Patton, and C. K. Morley, 1992, Rift-segment interaction and its relation to hydrocarbon exploration in continental rift systems: AAPG Bulletin, **76**, 1153–1169.

Okubo, C. H., and R. A. Schultz, 2006, Near-tip stress rotation and the development of deformation stepover geometries in mode II: GSA Bulletin, **118**, 343–348, doi: 10.1130/B25820.1.

Paul, D., and S. Mitra, 2013, Experimental models of transfer zones in rift systems: AAPG Bulletin, **97**, 759–780, doi: 10.1306/10161212105.

Philippon, M., E. Willingshofer, D. Sokoutis, G. Corti, F. Sani, M. Bonini, and S. Cloetingh, 2015, Slip re-orientation in oblique rifts: Geology, **43**, 147–150, doi: 10.1130/G36208.1.

Ramberg, H., 1981, Gravity, deformation and the earth's crust: Academic Press.

Rosendahl, B. R., 1987, Architecture of continental rifts with special reference to East Africa: Annual Review of Earth and Planetary Sciences, **15**, 445–503, doi: 10.1146/annurev.ea.15.050187.002305.

Rosendahl, B. R., E. Kilembe, and K. Kaczmarick, 1992, Comparison of the Tanganyika, Malawi, Rukwa and Turkana Rift zones from analyses of seismic reflection data: Tectonophysics, **213**, 235–256, doi: 10.1016/0040-1951(92)90261-4.

Saria, E., E. Calais, D. S. Stamps, D. Delvaux, and C. J. H. Hartnady, 2014, Present-day kinematics of the East African Rift: Journal of Geophysical Research: Solid Earth, **119**, 3584–3600, doi: 10.1002/2013JB010901.

Scholz, C. A., and D. R. Hutchinson, 2000, Stratigraphic and structural evolution of the Selenga Delta Accommodation Zone, Lake Baikal Rift, Siberia: International Journal of Earth Sciences, **89**, 212–228, doi: 10.1007/s005310000095.

Tentler, T., and V. Acocella, 2010, How does the initial configuration of oceanic ridge segments affect their interaction? Insights from analogue models: Journal of Geophysical Research, **115**, B01401, doi: 10.1029/2008JB006269.

Tron, V., and J.-P. Brun, 1991, Experiments on oblique rifting in brittle-ductile systems: Tectonophysics, **188**, 71–88, doi: 10.1016/0040-1951(91)90315-J.

Trudgill, B., and J. Cartwright, 1994, Relay-ramp forms and normal-fault linkages, Canyonlands National Park, Utah: Geological Society of America Bulletin, **106**, 1143–1157, doi: 10.1130/0016-7606(1994)106<1143:RRFANF>2.3.CO;2.

Ustaszewski, K., M. E. Schumacher, S. M. Schmid, and D. Nieuwland, 2005, Fault reactivation in brittle-viscous wrench system-dynamically scaled analogue models and application to the Rhine-Bresse transfer zone: Quaternary Science Reviews, **24**, 365–382, doi: 10.1016/j.quascirev.2004.03.015.

Weijermars, R., and H. Schmeling, 1986, Scaling of Newtonian and non-Newtonian fluid dynamics without inertia for quantitative modeling of rock flow due to gravity (including the concept of rheological similarity): Physics of the Earth and Planetary Interiors, **43**, 316–330, doi: 10.1016/0031-9201(86)90021-X.

Zwaan, F., G. Schreurs, J. Naliboff, and S. J. H. Buiter, 2016, Insights into the effects of oblique extension on continental rift interaction from 3D analogue and numerical models: Tectonophysics, **693 Part B**, 239–260, doi: 10.1016/j.tecto.2016.02.036.

Frank Zwaan received a B.S. (2010) in geology from the VU University Amsterdam and an M.S. joint degree (2013) from the VU University and the University of Rennes 1 (France), including an M.S. thesis project at Shell Oil Company. Currently, he is a Ph.D. candidate at the University of Bern (Switzerland), studying the effects of oblique extension and scissor tectonics on rift interaction and rift propagation with the use of analog models and X-ray CT techniques. His research interests include structural geology, (salt) tectonics, and (analog) modeling of associated processes, as well as seismic interpretation, basin analysis, petroleum geology, and sedimentary processes.

Guido Schreurs received an M.S. in geology from the University of Utrecht and a Ph.D. from the Institute of Geology at the ETH Zürich. He is a professor in geology and is head of the Tectonic Modeling Laboratory at the University of Bern (Switzerland). He also combines analog-modeling studies with field-based research in the sedimentary basins of western Madagascar to determine the impact of Paleozoic and Mesozoic opening kinematics on rifted margin architecture and evolution. His research interests include the influence of oblique extension on rift propagation and interaction using analog-model experiments analyzed by X-ray CT.